



A cell-free TLR5^{high} MSC membrane nanoparticle therapy for Crohn's disease: Targeted immunomodulation via the flagellin/TLR5 axis

Yuanyuan Xie^{a,b,1}, Yu Li^{c,1}, Congwang Xu^{a,1}, Wenting Zhang^{a,1}, Yue Jiang^b, Liudi Wang^b, Yingjie Tang^d, Qing Sun^a, Hui Yang^b, Xiaoli Mai^e, Pingping Shen^{c,*}, Bin Wang^{a,b,f,*}

^a Clinical Stem Cell Center, Nanjing Drum Tower Hospital, Clinical Medical College of Traditional Chinese and Western Medicine, Nanjing University of Chinese Medicine, Nanjing, Jiangsu Province 210009, China

^b Clinical Stem Cell Center, Nanjing Drum Tower Hospital, Affiliated Hospital of Medical School, Nanjing University, Nanjing, Jiangsu Province 210009, China

^c School of Life Science, Nanjing University, Nanjing, Jiangsu Province 210023, China

^d School of Pharmacy, China Pharmaceutical University, Nanjing, Jiangsu Province 211100, China

^e Department of Radiology, Nanjing Drum Tower Hospital, Affiliated Hospital of Medical School, Nanjing University, Nanjing, Jiangsu Province 210008, China

^f Jiangsu Key Laboratory for Molecular Medicine, Nanjing University, Nanjing, Jiangsu Province 210009, China

ARTICLE INFO

Keywords:

Inflammatory bowel disease
Mesenchymal stromal cells
Toll-like receptor 5
Biomimetic nanoparticles
Th1/Th17 immune dysregulation

ABSTRACT

Inflammatory bowel disease (IBD), including Crohn's disease (CD; Th1/Th17-driven) and ulcerative colitis (Th2-skewed), lacks therapies correcting T-cell imbalance. Current cytokine-focused treatments remain ineffective, while mesenchymal stromal cells (MSCs) therapies are hindered by inherent heterogeneity and challenges related to cell viability maintenance, batch-to-batch consistency, and standardization. This study aimed to (Kaplan, 2015 (1)) identify MSCs subtypes targeting CD pathology, Sebastian and Siegmund (2024) (2) create MSCs-mimicking nanoparticles, and (Li et al., 2016 (3)) propose a “deconstructed cell therapy” framework. Using colon datasets and CD blood samples, Th1/Th17-macrophage dysregulation was mapped. Transcriptomic screening of eight MSCs sources identified dental pulp-derived TLR5^{high}-MSCs as superior Th1/Th17 inhibitors compared to umbilical cord TLR5^{low}-MSCs. In colitis models, TLR5^{high}-MSCs intercepted gut flagellin (Fla), blocking macrophage TLR5/NF-κB to restore T-cell balance. Decellularized MSCs membranes were engineered into nanovesicles (TLR5^{high}-CMNP), which showed 3.7-fold higher Fla. affinity than antibodies and suppressed Th1/Th17 activity in vitro. In murine colitis, TLR5^{high}-CMNP achieved comparable efficacy to MSCs (e.g., 68.9 % reduction in MPO scores), while avoiding challenges associated with live-cell administration — such as embolism occurrence (0 % vs. 24 % in MSCs), need for viability maintenance, and potential variability in TLR5 expression.

Bioinformatic analysis confirmed TLR5 as pivotal for MSCs specificity, enabling tailored nanoparticle design. This study highlights TLR5^{high}-CMNP as a safer, cell-free MSCs alternative and introduces a paradigm prioritizing precise immune checkpoint targeting (e.g., Fla./TLR5) over broad cytokine suppression, resolving IBD therapeutic ambiguity through scalable biomimetic nanomaterials.

1. Introduction

Inflammatory bowel disease (IBD), encompassing Crohn's disease (CD) and ulcerative colitis (UC), constitutes a spectrum of chronic gastrointestinal disorders driven by distinct yet overlapping immunopathological mechanisms [1,2]. Ulcerative colitis is characterized by a Th2-skewed mucosal inflammation that typically originates in the rectum and progressively extends proximally. In contrast, CD is distinguished by its transmural lesions, predominantly affecting the terminal

ileum, and is associated with excessive activation of systemic T-helper type 1 (Th1) and Th17 immune responses [3,4]. These immune biases have been recapitulated in the 2,4,6-trinitrobenzene sulfonic acid (TNBS)-induced murine colitis model, which exhibits a Th1-dominant immune imbalance and clinical features reminiscent of CD, including diarrhea, weight loss, and hematochezia [5]. Although significant progress has been made in understanding the multifactorial etiology of IBD—encompassing dysbiosis, genetic susceptibility, and dysregulation of innate-adaptive immune interactions—the specific molecular drivers

* Corresponding authors.

E-mail addresses: ppshen@nju.edu.cn (P. Shen), wangbin022800@126.com (B. Wang).

¹ Yuanyuan Xie, Yu Li, Congwang Xu and Wenting Zhang contributed equally to this work.

<https://doi.org/10.1016/j.jconrel.2025.114121>

Received 24 April 2025; Received in revised form 20 July 2025; Accepted 11 August 2025

Available online 12 August 2025

0168-3659/© 2025 The Author(s). Published by Elsevier B.V. This is an open access article under the CC BY license (<http://creativecommons.org/licenses/by/4.0/>).

underlying pathological T-cell differentiation imbalance remain elusive [6,7]. Current therapeutic strategies primarily focus on symptom alleviation through conventional anti-inflammatory agents, small-molecule kinase inhibitors, or biologics targeting the TNF- α /IL-12/IL-23 axis. However, these approaches fail to address the fundamental causes of T-cell dysregulation and are often associated with systemic toxicity [8,9]. This critical unmet clinical need underscores the necessity for mechanism-driven therapeutic strategies capable of spatially and temporally precise modulation of mucosal immune homeostasis.

Mesenchymal stromal cells (MSCs), owing to their intrinsic immunoregulatory properties, tissue-homing ability, and multipotent differentiation plasticity, have emerged as a promising candidate therapy for IBD [10,11]. For a long time, MSCs have been regarded as outstanding candidates in regenerative and rehabilitative medicine, facilitating the repair of damaged tissues through their remarkable differentiation potential and leveraging their low immunogenicity and potent immunomodulatory properties for the treatment of autoimmune diseases [12]. Their therapeutic mechanisms are thought to operate primarily through three complementary pathways: paracrine signaling, extracellular vesicle (EV) transfer, and direct interactions with immune cells [13,14]. MSCs-based infusion therapies have demonstrated substantial potential in the treatment of IBD. Preclinical studies have shown that systemic MSCs infusion alleviates weight loss, improves colonic inflammation, and reduces disease activity indices (DAI) in IBD mouse models [15]. Moreover, as early as 2003, clinical trials successfully employed local MSCs injections to repair CD-associated rectovaginal fistulas [16]. However, several critical scientific challenges continue to hinder the optimization of MSCs therapy for IBD [17]. First, conventionally used MSCs — such as those derived from bone marrow (BM) — are administered based on their general “immunomodulatory potential” or “paracrine effects,” rather than through a disease-specific functional selection process, leading to inconsistent therapeutic outcomes when the same MSCs preparation is applied across multiple disease contexts [18]. Additionally, MSCs can be derived from various tissue sources, including adipose tissue (AD), BM, umbilical cord (UC), placenta, and dental pulp (DP), resulting in a source-dependent therapeutic effect [19]. Studies have reported significant differences in gene expression profiles, paracrine characteristics, and immunomodulatory efficacy among MSCs derived from different tissues, yet there remains no consensus on the optimal MSC source for IBD treatment [20]. Furthermore, general challenges associated with cell therapy, such as the therapeutic noise introduced by MSCs multipotency, further complicate clinical outcomes [21]. Although more than 50 immunomodulatory factors secreted by MSCs have been identified, issues including their short survival time (necessitating repeated administration), off-target effects (e.g., ectopic differentiation and genomic instability), and low engraftment efficiency at inflamed sites reduce the predictability of clinical outcomes [22–24]. This therapeutic ambiguity underscores a crucial principle: rather than treating MSCs heterogeneity as a limitation, it should be harnessed as a design feature [25]. By systematically matching disease-specific immunopathological checkpoints — such as the flagellin (Fla) / TLR5 axis identified in CD in this study — with functionally distinct MSCs subtypes, a mechanistically tailored approach to MSC-based cell therapy can be developed. The transition from universal MSCs to disease-matched MSCs represents a critical direction in the future development of MSC-based therapeutics. Additionally, transforming the complexity of live-cell therapy into well-defined, cell-free derivatives — such as the membrane nanovesicle particles designed in this study — offers a dual advantage [26]. On the one hand, it circumvents key limitations inherent to live-cell therapies — such as the need for cell viability maintenance, challenges in standardization, and variability in therapeutic factor expression. On the other hand, it preserves precise

immunotherapeutic properties, a paradigm we define as “deconstructed cell therapy.”

To identify an optimal MSC subtype targeted for CD pathophysiology and to develop effective cell-based therapeutic strategies that overcome key challenges associated with live MSC administration, this study was conducted at three levels. First, we leveraged large-scale single-cell RNA transcriptomic data from colonic biopsy samples of CD patients and healthy individuals, supplemented with clinical peripheral blood samples from CD patients to validate pathological alterations in T-cell subsets, revealing a dysregulated imbalance in pathogenic Th1/Th17 polarization. Next, we performed a comprehensive transcriptomic and phenotypic analysis of MSCs derived from eight distinct human tissue sources to investigate the key immunological dysregulation mechanisms of CD. Our findings demonstrated significant interindividual and tissue-specific heterogeneity among these MSC populations [27,28]. Notably, TLR5^{hi}-MSC, particularly DP-derived MSCs (DPMSC), were identified as a superior subtype capable of effectively suppressing pathogenic Th1/Th17 polarization imbalance (compared to UC-derived MSCs, which exhibited the lowest TLR5 expression, $p < 0.001$). The core regulatory network of TLR5^{hi}-MSC was found to be enriched in innate immune signaling pathways. Furthermore, using a modular macrophage-organoid co-culture system, we established a mechanistic link between TLR5 membrane abundance and macrophage reprogramming (M1-to-M2 transition). Literature reports indicate that in IBD patients, the proportion of pathogenic bacteria within the gut microbiota is increased, leading to a significant elevation in the release of specific pathogen-associated molecular patterns (PAMPs), including flagellin (Fla, a TLR5 ligand) and lipopolysaccharide (LPS, a TLR4 ligand) [29–31]. Notably, the detection rate of Fla-specific peptides (e.g., Fla-E) reached in active CD cases, compared to 25 % in controls ($p = 0.01$) [32]. Our study further elucidates that TLR5^{hi}-MSC competitively bind to the TLR5 ligand flagellin on the surface of intestinal mucosal macrophages, thereby intercepting the macrophage TLR5/NF- κ B signaling pathway and reprogramming systemic Th1/Th17 polarization, contributing to the restoration of T-cell homeostasis in CD model mice. Finally, through bioinformatics analysis, we identified membrane-associated proteins as key determinants of MSC immunomodulatory specificity. Comparative analysis between TLR5^{low}-MSC (UCMSC) and TLR5^{hi}-MSC (DPMSC) revealed that TLR5 plays a pivotal role in regulating T-helper cell balance. Notably, *in vitro* functional experiments demonstrated that decellularized MSC membrane components retained the essential immunoregulatory receptor TLR5, mirroring the immunosuppressive activity of their parental cells. This inherent molecular interaction with host immune cells effectively inhibited macrophage-driven M1 polarization-induced Th1 and Th17 proliferation. These findings inspire a paradigm shift from live cell therapy to cell membrane-derived nanoparticles (CMNP) — a biomimetic nanoplateform that replicates the hallmark features of MSC membranes (e.g., homing ligands and checkpoint regulators) while circumventing cell viability constraints (eliminating the need for cold-chain storage) and offering enhanced consistency and biosafety compared to live-cell preparations.

Based on the findings of our study, we engineered TLR5^{hi} biomimetic membrane nanovesicles (TLR5^{hi}-CMNP) and applied them in a preclinical TNBS-induced colitis model. These nanovesicles competitively bound Fla., thereby neutralizing the pathogenic TLR5/NF- κ B cascade and effectively mimicking the therapeutic functions of their parental MSCs. This study provides the first evidence demonstrating that: (1) MSCs membrane proteins (e.g., TLR5) serve as determinants of disease-specific therapeutic efficacy, challenging the conventional “cytokine-centric” paradigm in MSC-based therapies. (2) Bioengineered cell-free nanoparticles exhibit superior safety (e.g., no pulmonary retention)

and enhanced efficacy (e.g., sustained TLR5 antagonism) compared to their parental MSCs, addressing the “viability-efficacy paradox” of cell therapy. (3) A functional screening framework linking MSCs tissue characteristics with immune checkpoint biology enables the precise matching of therapeutic mechanisms to disease pathophysiology. By integrating systems biology with nanotechnology, we translate MSCs heterogeneity into target-defined biocompatible materials, overcoming long-standing challenges in the field of regenerative cell-based therapeutics.

2. Material and methods

The work has been reported in line with the ARRIVE guidelines 2.0.

2.1. Ethics statement

All experiments involving animals were conducted in compliance with relevant laws and approved by the Institutional Animal Care and Use Committee (IACUC) of Nanjing Drum Tower Hospital (Approval No 2020AE01094). All studies involved human samples complied with the Declaration of Helsinki and were approved by the Medical Ethics Committee of Nanjing Drum Tower Hospital (clinical research protocol number: 2020–245-01). All participants provided written informed consent.

2.2. Profiling and analysis of mRNA expression data

To explore the function of the Th cells and marker genes, public dataset of colon tissue from GEO was included. Sequencing dataset GSE266546 was analyzed and finally obtained 48 cases and 11 healthy controls. The ssGSEA in GSVA (version 1.44.5) was employed to quantify T cell signature levels per sample.

2.3. Clinical information

25 hospitalized patients with CD (10 males and 15 females, average age 52.1 years) were enrolled from Nanjing Drum Tower Hospital (Nanjing, China). Inclusion criteria for CD patients were: 1) fulfillment of the diagnostic criteria from the “Consensus on the Diagnosis and Treatment of Inflammatory Bowel Disease in China” (2018, Beijing, China), based on clinical manifestations, laboratory results, endoscopic findings, histopathological, and imaging evidence; 2) age over 18 years and the ability to consent. 20 healthy controls (8 males and 12 females, average age 48.0 years) were enrolled from the Health Examination Center of Nanjing Drum Tower Hospital. Inclusion criteria for healthy controls were: 1) healthy volunteers; 2) age over 18 years and the ability to consent. All participants provided written informed consent. The study was approved by the Medical Ethics Committee of Nanjing Drum Tower Hospital under the project titled “TLR5(high)-MSC Improve Inflammatory Bowel Disease by Regulating Th1/Th17 Subtypes” (clinical research protocol number: 2020–245-01), with approval granted on April 5, 2020.

2.4. Isolation, expansion and culture of PBMCs derived from peripheral blood

Approximately 10 ml of peripheral blood (PB) was collected from each participant (patients and healthy controls). The PB samples were then centrifuged at 3,500 rpm for 10 min using a cryogenic high-speed centrifuge (Eppendorf, Germany), which separated the serum layer for subsequent cytometric bead assay (CBA, BD, USA). To isolate peripheral blood mononuclear cells (PBMCs), density gradient centrifugation was performed using Lymphoprep (Axis-Shield, AS1114546, Norway). The

isolated PBMCs were resuspended in Roswell Park Memorial Institute (RPMI) 1640 medium (C11875500BT, Gibco, USA) supplemented with 10 % fetal bovine serum (FBS, 10099141C, Gibco, USA) and 1 % penicillin-streptomycin solution (15140122, Gibco, USA), and cultured at 37 °C in a 5 % CO₂ atmosphere for further analysis.

2.5. Isolation, expansion and identification of clinical-grade MSC derived from eight tissues

All samples for MSC isolation in this study were obtained from donors at Nanjing Drum Tower Hospital. Informed consent was obtained from each participant, and the study was approved by the Institutional Review Board (Project title: “Utilization of Clinical Patient Samples (Tissue/Blood/Body Fluids) and Aborted Fetal Tissue to Extract Stem Cells for Basic and Clinical Research in Regenerative Medicine and Treatment of Clinical Diseases”; Approval No. 2017–161-08; Approval Date: November 30, 2017).

Bone marrow aspirates were collected from patients undergoing orthopedic surgery, and mononuclear cells were isolated using density gradient centrifugation. The method for isolating bone marrow-derived MSC (BMMSC) was adapted from a previous study [33]. Fresh UC segments, approximately 15 cm in length, were obtained from full-term infants to isolate primary UCMSC via tissue grafting methods [34]. Adipose tissue samples were acquired from elective plastic surgeries, while dental pulp samples were obtained from exfoliated deciduous incisors of children aged 7 to 8 years. Gingival tissue samples were collected from healthy adults undergoing orthodontic surgery. Chorion, amnion, and meconium samples were obtained from the same full-term placenta. Primary MSC from adipose tissue (ADMSC), dental pulp (DPMSC), gingival tissue (GMSC), placental villous tissue (PCMSC), amnion (AMSC), and decidua (DMSC) were isolated using digestive enzyme culture methods as described in previous reports [35–38]. Detailed experimental methods and regulations are outlined in our previous publication [39]. All MSCs were processed in GMP-certified cell centers according to strict Standard Operating Procedures (SOPs) and underwent thorough quality control to meet clinic-grade MSC criteria [39].

The detailed experimental reagents and methods for MSC phenotype identification, multilineage differentiation potential assessment, and immune function suppression (including Th1/Th17/Treg differentiation) could be referred to our previous research [25].

2.6. MSC culture and population doubling time assays

MSCs were cultured in Dulbecco's Modified Eagle Medium (DMEM) (10567014, Gibco, USA), supplemented with 10 % fetal bovine serum (FBS) (10099141C, Gibco, USA) and 1 % penicillin-streptomycin solution, at 37 °C in a 5 % CO₂ atmosphere. To eliminate individual variations, a 1:1:1 ratio of clinic-grade UCMSC derived from three donors (UC-1, UC-2, UC-3) was used, and the mixture was designated as UCMSC for subsequent experiments. A similar approach was used for clinic-grade DPMSC derived from three donors (DP-1, DP-2, DP-3), which were mixed at a 1:1:1 ratio and referred to as DPMSC. All MSCs were maintained between passages 3 and 8 to prevent cellular senescence.

The population doubling of each MSC type was monitored by counting the total cell number at each passage during subculture. The difference in cell number from the harvest stage was calculated using the formula: $[\log_{10}(N) - \log_{10}(N_0)] / \log_{10}(2)$, where N is the number of cells at passage, and N₀ is the initial cell number. Population doubling time was calculated using the formula: $(t - t_0) \bullet \log_2 / \log(N - N_0)$, where (t - t₀) represents the culture time (h), N is the number of harvested cells, and N₀ is the initial cell number [40].

2.7. RNA isolation, library preparation, and sequencing analysis

OE Biotech Co. Ltd. (Shanghai, China) conducted RNA extraction and processing, libraries construction and transcriptome sequencing and analysis. (1) Preparation for RNA-sequencing data: Read counts for each gene were quantified, and Transcripts Per Million (TPM) were calculated. Low-expression genes with TPM < 1 in all of samples or mean TPM < 0.5 were then excluded. All expression values were log-transformed. (2) The basic genetic visualization of genes: In *seurat*, t-distributed stochastic neighbor embedding, the nonlinear dimension reduction method, was used to map high dimensional gene expression data into a three-dimensional space, bringing together samples with similar expression patterns. The differences between the samples were thus made more comprehensible. (3) The pathways of biological process were selected from the R package *clusterProfiler* (version 4.12.1). The single sample gene set enrichment analysis (ssGSEA) implemented in the R package *GSEA* (version 1.44.5) was used to quantify the infiltrate levels of pathways for each sample with expression data [41]. Differential gene set enrichment across 8 tissues was evaluated using ANOVA, and multiple comparisons were performed using the Tukey's honestly significant difference. (4) Differential gene expression analysis: The 'DESeq2' package was utilized to identify differential genes (DEGs) among UCMSC and DPMSC. False discovery rate (FDR) method was applied to correct the results at $p < 0.05$ level. The screening criteria was $|\log_2 \text{fold change}| > 1$. By using KEGG pathway significant enrichment analysis, we analyzed the biological functions of the differential expressed genes [42]. (5) Correlation of cell membrane genes and Th1-related genes: First, we go through all the proteins corresponding to the genes in our data to confirmed the cell membrane genes from the UniProt resources (<https://www.uniprot.org>) by the R package *UniprotR* [43]. Then, we conducted the correlation analysis between cell membrane genes and Th1-related genes using the Pearson correlation test from the expression matrix, corrected the results at $p < 0.05$ level by FDR method.

2.8. Generation of TLR5 knockdown MSC with siRNA

siRNA-TLR5 was purchased from Hippo Biotechnology. To generate TLR5-deficient MSC, 50 nM siRNAs were transfected into MSC using RNAiMAX (Invitrogen, 13778-075, USA) at a 1:3 siRNA-to-reagent ratio, following the manufacturer's protocol, when the MSC reached 60–70 % confluence. The efficiency of TLR5 knockdown was assessed 72 h post-transfection. MSC were then used in subsequent experiments 24 h after transfection.

2.9. Quantitative real-time PCR analysis

Total RNA was extracted from MSC, PBMCs, and THP-1 cells using *VeZol* reagent (Vazyme, R411-02, China), according to the manufacturer's instructions. RNA concentration was quantified using a *NanoDrop™ One Microvolume UV-Vis Spectrophotometer* (Thermo Fisher Scientific). Complementary DNA (cDNA) was synthesized by reverse transcription of 1 µg of RNA using *Hicript III Reverse Transcriptase*. Quantitative PCR (qPCR) was performed with 2 µl of cDNA, 1 µl of forward and reverse primers, 10 µl of *ChamQ SYBR qPCR Master Mix* (Vazyme, Q311-02, China), and 6 µl of ddH₂O on a *QuantStudio™ 6 Flex Real-Time PCR System* (Applied Biosystems), followed by melting curve analysis. Results were normalized to glyceraldehyde 3-phosphate dehydrogenase (GAPDH) expression. Data were analyzed using the comparative Ct ($2^{-\Delta\Delta Ct}$) method and further normalized to the negative control. Primer sequences for the reactions are listed in Supplementary Table 1.

2.10. TNBS-CD model and MSC (or MSC - CMNP) transplantation

C57BL/6 mice (female, 22–25 g, 8–9 weeks old) were purchased from Nanjing Charles River Laboratories. Prior to TNBS treatment, all mice were fasted for 24 h with free access to water. On day 0 (D0), experimental CD models were established by intra-rectal injection of 100 µl TNBS (5 % w/v TNBS: absolute ethanol = 1:1; Sigma-Aldrich, USA) 3–4 cm into the colon lumen under anesthesia with 1 % isoflurane (RWD, R510-22-10, China).

In the *in vivo* treatment study, the treatments included intraperitoneal injection of PBS (300 µl), 1×10^6 UC/DP-MSC, 1×10^6 UC/DP (SiNC/SiTLR5)-MSC, or 200 µg UC/DP-CMNP at hour 6, and caudal vein injection of PBS (300 µl), 5×10^5 UC/DP-MSC, 5×10^5 UC/DP (SiNC/SiTLR5)-MSC, or intraperitoneal injection of 100 µg UC/DP-CMNP at hour 24 after TNBS modeling. Mice were then euthanized by overdose of anesthesia (5 % isoflurane) on day 4 post-induction, and spleen, mesenteric lymph node, and colon tissues were collected for subsequent analysis. All procedures were approved by the Institutional Animal Care and Use Committee (IACUC) of Nanjing Drum Tower Hospital.

2.11. MSC biodistribution analysis

Mice were induced to develop CD and subsequently received UCMSC/DPMSC via tail vein injection, as previously described. To trace Green Fluorescent Protein (GFP)-MSC, 5×10^5 UCMSC or DPMSC genetically engineered to overexpress GFP were injected into TNBS-CD mice in 0.3 ml PBS. For CM-DiI staining (Thermo Fisher, USA), UCMSC or DPMSC were digested, centrifuged, and resuspended in 1 ml CM-DiI dye. Cells were incubated at 37 °C for 15 min and at 4 °C for an additional 15 min. A total of 5×10^5 CM-DiI-stained UCMSC or DPMSC in 0.3 ml PBS were then injected into TNBS-CD mice. At 0, 6, 24, 48, and 72 h post-transplantation, mice were euthanized, and colon tissues were collected for detection of GFP-positive and CM-DiI-positive cells. The distribution of transplanted MSC was traced using fluorescence confocal microscopy.

2.12. Assessment of IBD

Each experimental mouse was weighed and monitored daily for the occurrence of diarrhea, bloody stool, and weight loss. The DAI was calculated according to the scoring criteria provided in Supplementary Table 2.

In the TNBS-induced CD mouse model, the distal colon was excised from each mouse and fixed in 4 % phosphate-buffered paraformaldehyde overnight for histological analysis. Each sample was embedded in paraffin, sectioned either horizontally or vertically, and stained with H&E. Histological images were captured using an optical microscope (Olympus BX51, Olympus Corporation). The microscopic inflammation score (MIO) was determined based on the H&E results and two parameters outlined in Supplementary Table 3. Additionally, samples were stained with Periodic Acid-Schiff (PAS) and myeloperoxidase (MPO) to assess changes in goblet cell number and neutrophil infiltration in the colon.

2.13. Lymphocytes isolation from spleen and MLN

All mice were euthanized, and the spleens and mesenteric lymph nodes (MLN) were aseptically harvested, ground, and filtered through a 45 µm nylon membrane. The resulting lymphocytes were isolated from these tissues. The filtered cells were then resuspended in RPMI 1640 medium supplemented with 10 % heat-inactivated FBS (incubated at 65 °C for 30 min), 100 U/ml penicillin, and 100 µg/ml streptomycin,

and the cell concentration was adjusted as needed. The lymphocytes from both tissues were grouped and stimulated with a cocktail. One group was stimulated for 4 h for RNA extraction and Q-PCR analysis, while another group was stimulated for 5 h for flow cytometry (FCM) analysis.

2.14. THP-1 cell culture and macrophage differentiation

THP-1 cells were cultured in RPMI 1640 medium supplemented with 10 % FBS (10099141C, Gibco, USA) and 1 % penicillin-streptomycin solution (15140122, Gibco, USA) at 37 °C in a 5 % CO₂ atmosphere. The cells were then induced with 50 ng/ml phorbol 12-myristate 13-acetate (PMA, Sigma, USA) for 24 h to differentiate into mature macrophages. Subsequently, the cells were cultured in fresh RPMI 1640 medium for an additional 24 h, resulting in the formation of adherent M0 macrophages for subsequent experiments.

2.15. In vitro effects of MSC on the regulation of macrophage

A density of 5×10^5 undifferentiated THP-1 monocytes per well was seeded into 12-well plates and adhered with PMA, as previously described. Simultaneously, MSCs were placed in 0.4 µm pore size 12-well transwell inserts (Corning, USA). After 24 h, THP-1 cells were induced into macrophages, and flagellin (100 ng/ml, Sigma, SRP8029, USA) was added to the media for an additional 24-h incubation. The cytokines in the supernatant were then collected and quantified using CBA. Macrophages and MSCs were then used for protein extraction to detect the expression of TLR5 and the phosphorylation levels of the IκBα and MAPK signaling pathways by Western blot.

2.16. Cytometric Beads assay

Cytokine concentrations (IL-8, IL-1β, IL-6, IL-10, TNF-α, and IL-12p70) were measured using a Cytometric Bead Array (CBA) kit (BD, 551811, USA), following the manufacturer's protocol. Cytokine intensities were then detected by FCM, and the resulting data were analyzed using graphical user interface software.

2.17. Macrophage depletion in TNBS induced CD mice

Macrophage depletion in TNBS-induced CD mice was achieved using Clodronate Liposomes (YEASEN, 40337ES10, China). For this purpose, each mouse received an intravenous injection of 200 µl control liposomes (PBS) or clodronate liposomes under anesthesia with 1 % isoflurane (RWD, R510-22-10, China) one day before TNBS treatment (D-1) and two days after TNBS treatment (D2). Mice were divided into four groups: (1) IBD: mice treated with TNBS, control liposomes (PBS), and PBS; (2) IBD + Clo: mice treated with TNBS, clodronate liposomes, and PBS; (3) Clo + UCMSC: mice treated with TNBS, clodronate liposomes, and UCMSC; (4) Clo + DPMSC: mice treated with TNBS, clodronate liposomes, and DPMSC. Mice were then euthanized by overdose of anesthesia (5 % isoflurane) on day 4 post-induction, colon tissues were collected for subsequent analysis, spleens and MLN were processed into single-cell suspensions. These were treated with erythrocyte lysate (Solarbio, R1010) and incubated with CD11b-PerCP and F4/80-FITC antibodies (BD Biosciences) to verify macrophage depletion (CD11b⁺ F4/80⁺) by FCM. All procedures were approved by the Institutional Animal Care and Use Committee (IACUC) of Nanjing Drum Tower Hospital.

2.18. Preparation and characterization of CMNP

The MSC membrane was isolated using a hypotonic lysis method [44]. MSCs were cultured until approximately 80 % confluency was reached, then detached with 0.25 % trypsin/EDTA (Gibco, USA). The cells were collected and resuspended in a hypotonic lysate solution containing 10^{-3} M phenylmethanesulfonyl fluoride, 10^{-3} M KCl, 1.5×10^{-3} M MgCl₂, and 10^{-2} M Tris-HCl (pH 8.0). The cell suspension was rapidly frozen in liquid nitrogen at -196 °C, followed by thawing at room temperature (15–25 °C) for 4–5 cycles. The mixture was then centrifuged at 4 °C at 850 ×g for 10 min. The supernatant was collected, and a second centrifugation step at 15,000 ×g for 30 min was performed to obtain precipitates containing MSC membranes. Membrane proteins were quantified using the Pierce BCA protein assay kit (Vazyme, China). Finally, the extracted membrane mixture was extruded through a 200 nm membrane filter to obtain MSC-CMNP.

The morphology of the MSC-CMNP was confirmed using transmission electron microscopy (TEM). For TEM imaging, MSC-CMNP samples were placed on copper grids, stained with 2 % ammonium molybdate, and air-dried prior to examination with a Hitachi microscope. To visualize the MSC-CMNP, they were labeled with Dio (Beo Tianmei Biotechnology Co., Ltd., China) and observed with a Leica laser scanning confocal microscope. The IgG isotype was used as a negative control. CMNP samples were then incubated with MSC membrane protein markers (CD45, CD105, CD73, and CD90) and analyzed by FCM. Dynamic light scattering (DLS) was used with a Malvern Zetasizer instrument to determine the hydrodynamic diameter of the nanoparticles. The expression of MSC markers (CD90) and exosome markers (Calnexin, TSG101 and CD81) was assessed to confirm the retention of cell membrane characteristics.

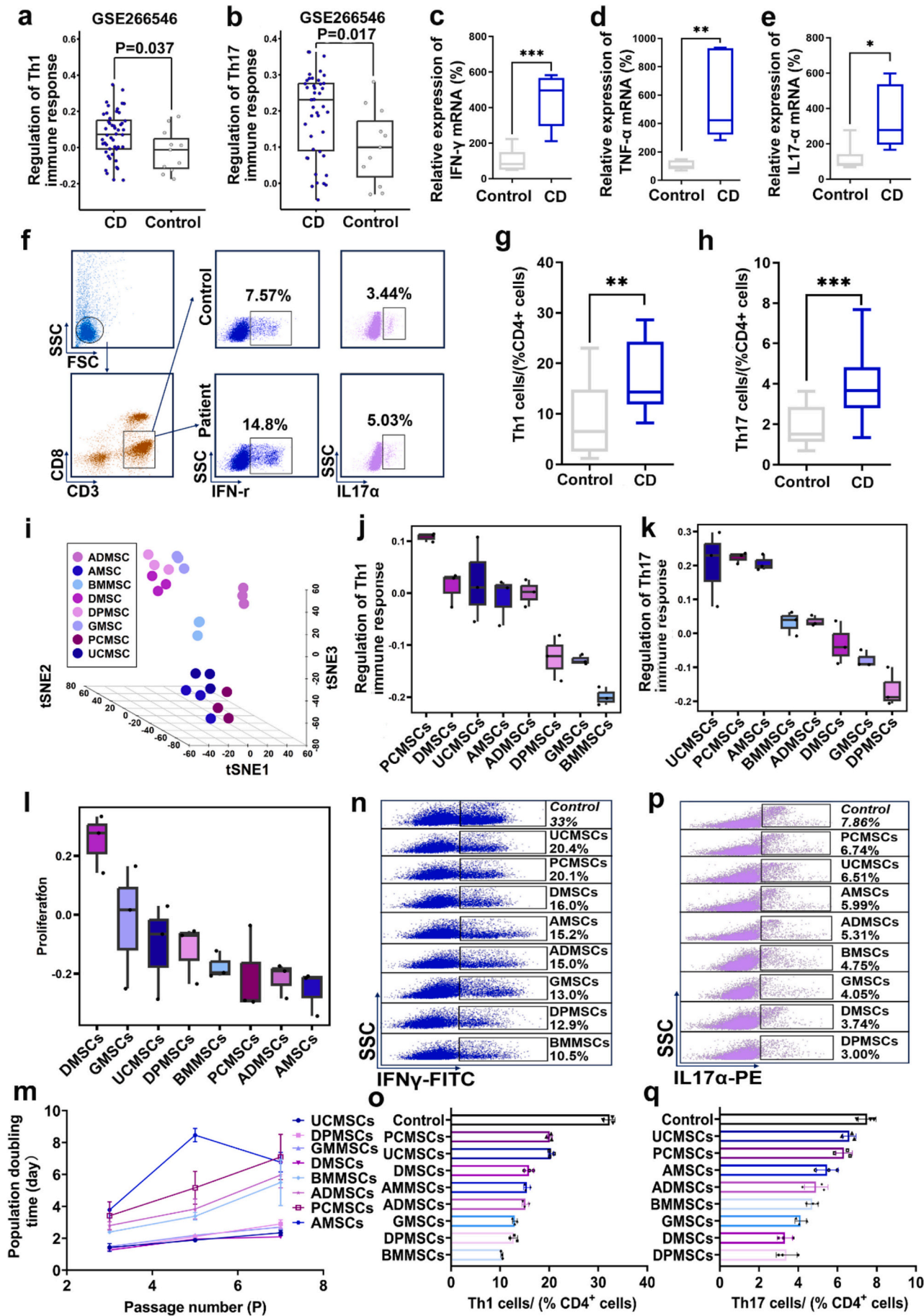
2.19. Zeta potential

A Zetasizer Nano Series (Zen 3600) (Malvern Panalytical, Worcestershire, United Kingdom) was used for zeta potential (mV) measurement on MSC-CMNP. The samples were kept at room temperature before performing the measurements. 10 µl of the sample was added to 1 ml of 0.1 µm filtered deionized water and loaded in a disposable capillary cell (DTS1070, Malvern Panalytical, Worcestershire, United Kingdom). The analysis temperature for the machine was set at 25 °C. The refractive index was manually set to 1.390, absorption to 0.01, and water set as a dispersant. The equilibration time was set to 60 s. Three measurements were set for each run. Before doing the experiment, the machine was calibrated using a ZTS1240 zeta potential transfer standard solution (Malvern Panalytical, Worcestershire, United Kingdom).

2.20. In vitro CMNP-mediated immune modulation

UC/DP-CMNP was added to the culture system of Fla-stimulated adherent M0 macrophages and cell supernatants were collected at 24 h after co-culture for culturing PBMCs to detect their immunomodulatory effects on Th1 and Th17, while macrophages were incubated with antibodies against CD11b-FITC and CD86-PE and assayed by FCM to detect their polarization towards the M1 phenotype.

To visualize THP-1 competing with MSC-CMNP for Fla. binding, we labeled THP-1 cells with CMDiI (Invitrogen, USA) and self-coupled Fla. to APC fluorescence (Invitrogen, USA) following the manufacturer's protocol. CMNP was then assayed by FCM to determine its specific binding efficiency to Fla-APC after treatment with anti-TLR5 antibody. The overlap of red and blue colors observed by Leica laser scanning confocal microscope indicates binding of THP-1 to Fla. Changes in the percentage of Fla-APC after co-culture with THP-1 and CMNP, which



(caption on next page)

Fig. 1. Heterogeneity-Guided MSC Selection for Precision Immunomodulation in CD. (a-b) Transcriptional meta-analysis of CD cohorts (GEO: GSE206171) identifies enhanced Th1/Th17 polarization signatures in CD patients versus healthy controls. (c-e) qPCR validation of Th1/Th17-associated cytokines (IFN- γ , TNF- α , IL17- α) in peripheral blood mononuclear cells (PBMCs) from CD patients, confirming systemic inflammatory escalation. (f-h) Flow cytometric quantification of activated CD3⁺CD8⁺ IFN- γ ⁺ (Th1) and CD3⁺CD8⁺ IL-17 A⁺ (Th17) subsets in CD PBMCs, illustrating disease-specific T-cell dysregulation. (i) RNA sequencing was performed on MSC derived from eight different tissues, and principal component analysis was conducted to analyze the gene expression of 24 samples from these tissues. (j-k) Functional profiling of MSC immunomodulatory capacity across eight tissue origins, revealing source-dependent variability in Th1/Th17 suppression. (l-m) Genomic differences in MSC proliferation from eight tissues and population doubling time analysis. (n-q) Representative flow cytometry plots showing the inhibitory effect of MSC from eight tissues on the proliferation of CD3⁺CD8⁺ IFN- γ ⁺ (Th1) and CD3⁺CD8⁺ IL-17 A⁺ (Th17) subsets in CD patients PBMCs, along with corresponding statistical analyses. Unpaired *t*-test was used to determine *p* values (**p* < 0.05; ***p* < 0.01; ****p* < 0.001).

were analyzed by FCM, provided evidence for the same effect.

2.21. FCM

The supernatant of PBMCs in the PBMC/MS (or PBMC/MS-FCMNP) co-culture system was collected, centrifuged, and stimulated with the Cell Stimulation Cocktail (Invitrogen, 00-4975-93, USA) at 37 °C for 5 h. To detect the percentage of Th1 (CD3⁺CD8⁺ IFN- γ ⁺), Th17 (CD3⁺CD8⁺ IL-17 A⁺), and Th2 (CD3⁺CD8⁺ IL-4⁺) cells, PBMCs were stained with surface antibodies CD3-PerCP, CD8-APC, and intracellular cytokine antibodies IFN- γ -FITC, IL-17 A-PE, and IL-2-BV410 (BD Biosciences, USA), followed by flow cytometry (FCM) analysis. MSC fragments (2.5 × 10⁴ cells per well) were seeded in 24-well plates. The following day, PBMCs were labeled with CFSE (eBioscience, 65-0850-84, USA) and co-cultured with MSC (lysate) in the same plates. After 3 days, PBMCs were collected for further analysis.

Lymphocytes dissociated from spleen and MLN tissues were incubated with CD4-FITC, IFN- γ -PE, IL-17 A-PE, and IL-4-APC antibodies (BD Biosciences, USA) for surface and intracellular cytokine staining. The percentage of Th1 (CD4⁺ IFN- γ ⁺), Th17 (CD4⁺ IL-17 A⁺) and Th2 (CD4⁺ IL-4⁺) cells was analyzed by FCM. Unstained cells were acquired (10,000 events) to set the gate for positively labeled cells.

All samples were analyzed using a flow cytometer (BD Accuri™ C6 Plus, USA), and data were processed using FlowJo software version 10.

2.22. SDS-PAGE and immunoblotting

For immunoblotting, 1 × 10⁶ cells were seeded per well in a 24-well plate, differentiated, and stimulated as described above. Cells were washed with ice-cold PBS and lysed on ice for 15 min in 250 μ l of RIPA buffer (Beyotime, P0013B, China) supplemented with 100 × protease inhibitors (Beyotime, P1005, China) and 50 × phosphatase inhibitors (Beyotime, P1081, China). Lysates were cleared by centrifugation at 12,000 ×g for 25 min at 4 °C. Protein concentrations were determined using the BCA assay (Vazyme, E112-02, China). Fifteen to twenty μ g of total protein per sample was mixed with 5 × loading dye (Beyotime, P0015, China), denatured at 95 °C for 10 min, and separated by SDS-PAGE.

After SDS-PAGE, proteins were transferred onto methanol-activated PVDF membranes (Beyotime, FFP39, China) using wet transfer at 300 mA for 1 h in Towbin buffer (25 mM Tris-HCl, pH 8.3, 192 mM glycine, 20 % (v/v) methanol). Depending on the primary antibody, membranes were blocked with 5 % BSA or 5 % non-fat dry milk in TBST (0.05 % Tween-20) for 60 min at room temperature. Membranes were incubated overnight at 4 °C with primary antibodies against GAPDH (1:300,000, Abclonal, A19056, China), TLR5 (1:2,000, Abcam, ab13876, USA), IKB α (1:5,000, Abcam, ab32518, USA), P-IKB α (1:1,000, CST, 2859 T, USA), JNK (1:1,000, Proteintech, 66210-1-Ig, China), P-JNK (1:1,000, Beyotime, AF1762, China), ERK (1:1,000, Proteintech, 16443-1-1AP, China), P-ERK (1:1,000, Beyotime, AF1891, China), P38 (1:1,000, Proteintech, 14064-1-AP, China), P-P38 (1:1,000, Abcam, ab133462, USA),

Calnexin (1:1,000, Abcam, ab133615, USA), TSG101 (1:2,000, Abcam, ab125011, USA), CD81 (1:1,000, Abcam, ab109201, USA), and CD90 (1:2,000, Abcam, ab307736, USA). Blots were developed by washing with TBST, probing with 1:2,000 diluted HRP-conjugated secondary antibodies, washing again, and then imaging with an enhanced chemiluminescence system (Biosharp, BL523B, China). For reprobing, membranes were stripped using a Western blot stripping buffer (NCM, WB6500, China). Densitometric analysis of protein band intensities were performed using ImageJ/Fiji (v.2.14.0), and results were normalized to the loading control.

2.23. Colon tissue immunofluorescence staining

Colon tissue samples were fixed in 4 % paraformaldehyde at 4 °C, followed by dehydration, embedding in optimal cutting temperature (OCT) compound and then frozen. Tissue sections (6 μ m) were prepared using a cryostat and mounted onto glass slides. For staining, slides were fixed in pre-chilled methanol (−20 °C) for 30 min, followed by three washes (5 min per wash) with 4 °C pre-cooled PBS. Sections were permeabilized in PBS containing 0.1 % Triton X-100 for 20 min at room temperature and rinsed three times with PBS. To block nonspecific binding, slides were incubated with 5 % FBS (diluted in PBS) for 30 min. Primary antibodies targeting CD86 (1:100, Abcam, ab119857, USA) and Arg-1 (1:500, Proteintech, 16001-1-AP, China) were diluted in 5 % FBS and applied to the sections overnight at 4 °C. After three PBS washes, sections were incubated with species-matched secondary antibodies conjugated to Alexa Fluor™ 488 (1:500, Invitrogen, A11006, USA) and Alexa Fluor™ 568 (1:500, Invitrogen, A11011, USA) for 1 h in the dark. Slides were washed again with PBS and then the excess liquid was carefully wiped away. Finally, the sections were mounted using an anti-quenching mounting medium containing DAPI.

2.24. Isolation and detection of human primary macrophages (pM ϕ)

Following PBMC isolation, the cells were washed and resuspended in PBS containing 4 % HSA and 0.5 mM EDTA. Monocytes were then isolated using CD14 MicroBeads (130-050-201, Miltenyi Biotec, Germany) in accordance with the manufacturer's protocol.

In summary, the PBMCs utilized for CD14^{pos} selection were diluted to a concentration of 1 × 10⁷ cells/ml and then incubated with 20 μ l CD14 MicroBeads for 15 min at 4 °C. The PBMC suspension was subsequently loaded onto a MACS column and positioned within the magnetic field of a MACS separator. The magnetically labeled CD14⁺ monocytes are retained within the column, while the unlabeled cells pass through. Following the removal of the column from the magnetic field, the magnetically retained CD14⁺ monocytes were washed in PBS with 4 % HSA and 0.5 mM EDTA. The cells were subsequently resuspended in RPMI-1640 containing 10 % FBS, 1 % PS and 50 ng/ml M-CSF (300-25, PeproTech, USA), and then placed in the incubator for macrophages differentiation. The media were changed every 2 days.

In order to detect the purity of CD14⁺ monocytes, 3 × 10⁴ cells/tube were stained with surface antibodies: CD11b-PerCP, CD45-APC, and

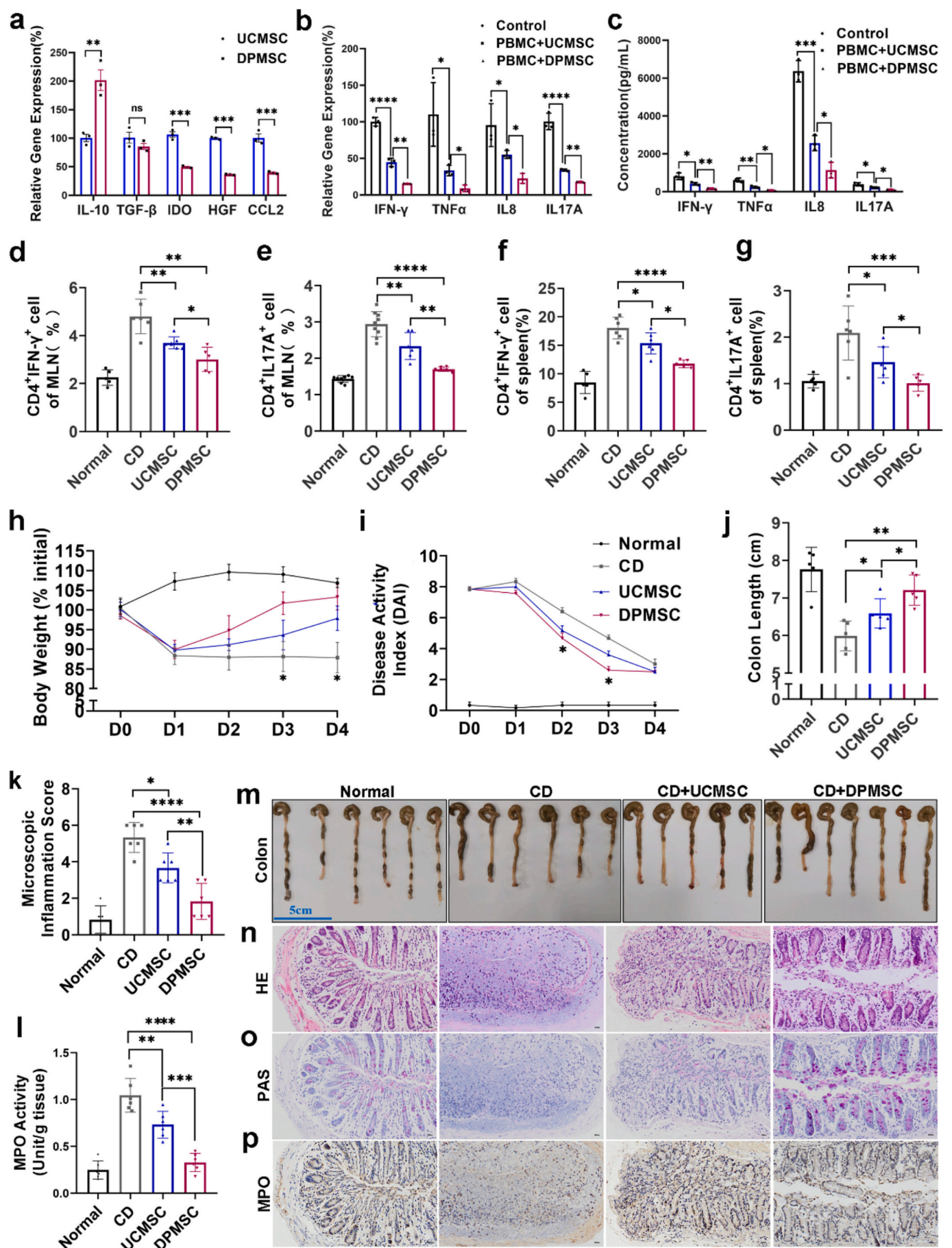


Fig. 2. Source-Dependent Immunomodulatory Divergence of UCMSC and DPMSC: Mechanistic Profiling and Therapeutic Stratification in IBD Models. (a) Statistical analysis of immune-related gene expression (IL-10, TGF- β , IDO, HGF, CCL2) between UCMSC and DPMSC. (b-c) Functional cytokine suppression profiles of UCMSC versus DPMSC in PBMCs cocultures: Differential inhibition of Th1 (IFN- γ , TNF- α) and Th17 (IL-8, IL-17 A) effector molecules (MSC-dominated suppression). (d-g) Flow cytometric analysis of proinflammatory T-cell subsets (Th1: CD4⁺IFN- γ ⁺ and Th17: CD4⁺IL-17 A⁺) in MLN (d-e) and splenic (f-g) from TNBS-induced CD mice. DPMSC administration significantly suppressed Th1 and Th17 responses compared to UCMSC treatment. Statistical significance was determined using ANOVA followed by Tukey's post hoc test. Data are presented as means \pm SD ($n = 5-7$ biologically independent samples). (h-l) Comparative efficacy analysis of colon length, MPO activity kinetics, body weight, and DAI in treated mice. DPMSC-treated mice displayed markedly reduced MPO and MIO versus UCMSC controls. (m-p) Representative images and pathological staining results (colon length, HE, PAS and MPO) of mouse colon tissues after different treatments. Statistical significance determined by one-way ANOVA (* $p < 0.05$, ** $p < 0.01$, *** $p < 0.001$).

CD14-FITC. Subsequent analysis was conducted via FCM.

2.25. Evaluation of TLR5-mediated pM ϕ polarization and downstream PBMC responses

After monocyte-derived macrophages differentiation, the cells were stimulated with different treated MSCs CMNP (UC-SiNC-CMNP/ UC-SiTLR5-CMNP) or left untreated for 24 h. Subsequently, the cells were digested with trypsin, resuspended in PBS and stained with surface antibodies: CD11b-PerCP, CD86-PE, and CD206-APC. FCM analysis was then performed to determine the ratio of M1/M2 macrophages.

Following monocyte-to-macrophage differentiation, the cells were co-cultured for 48 h with MSCs CMNPs, including UC-SiNC-CMNP, UC-SiTLR5-CMNP, DP-SiNC-CMNP, or DP-SiTLR5-CMNP, in the presence of Fla. For the TLR5 blockade group, CMNPs were pre-incubated with an anti-TLR5 neutralizing antibody prior to co-culture. After 48 h, macrophage polarization was assessed. Culture supernatants from each group were subsequently collected and used to stimulate PBMCs for 72 h. FCM was performed to evaluate the proportions of Th1 and Th17 subsets in PBMCs.

Adherent macrophages were harvested by trypsin digestion and resuspended in PBS, followed by surface staining with CD11b-PerCP, CD86-PE, and CD206-APC antibodies. The M1/M2 macrophage ratio was then determined by FCM analysis.

2.26. Statistical analyses

GraphPad Prism version 10.0.0 for Windows (GraphPad Software Inc., Boston, MA, USA, www.graphpad.com) was used for statistical analysis. All data are presented as mean \pm standard deviation (SD). Parametric methods were used for normally distributed data. Nonparametric methods, such as the Mann-Whitney U test with Dunn's post hoc analysis, were used for data that were not normally distributed. For data satisfying the homogeneity of variance criteria, independent samples t -test or two-way analysis of variance with Tukey's post hoc test or least significant difference test were used. All statistical tests were two-tailed with a type I error rate fixed at $\alpha = 0.05$. Experimenters remained unaware of group assignments and outcomes throughout the research. p values below 0.05 were deemed significant, with significance thresholds set at * $p < 0.05$, ** $p < 0.01$, *** $p < 0.001$, **** $p < 0.0001$.

3. Results and discussion

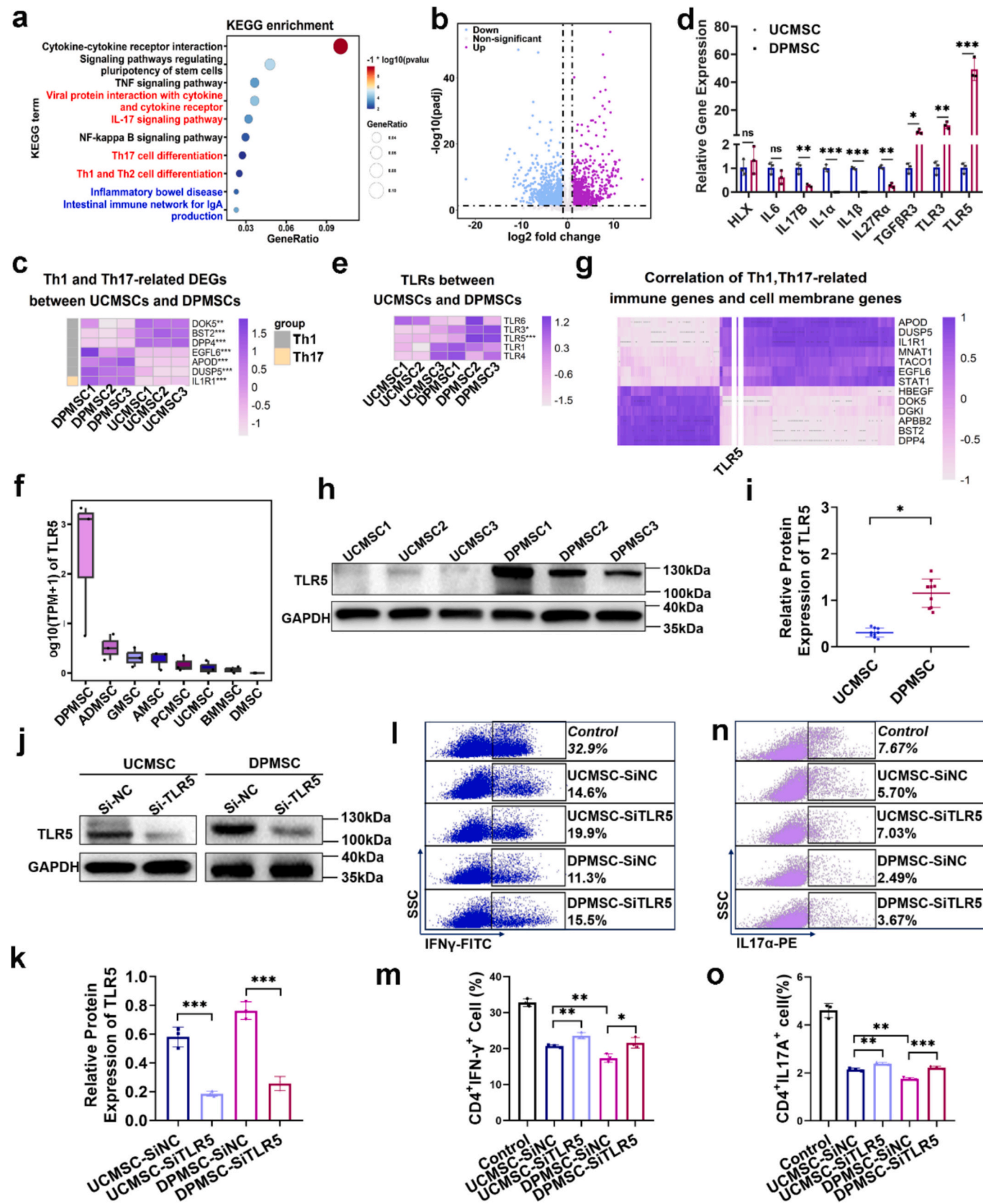
3.1. Tissue-specific MSC screening identifies DPMSC with superior Th1/Th17 immunoregulatory capacity in CD

At the outset of the study, RNA sequencing data were analyzed to investigate the pathogenesis of CD. Analyses of CD pathogenesis revealed a pathological Th1/Th17 polarization signature, with RNA-seq demonstrating upregulation of Th1 immune response and Th17 immune response in patient colonic mucosa versus healthy controls (HCs; $p =$

0.037, $p = 0.017$, Fig. 1a-b). To further validate these findings, PB was collected from patients, and PBMCs were isolated for subsequent testing. Systemic validation in PBMCs from 25 CD patients confirmed elevated Th1/Th17 frequencies by immunoreactive genes in PBMCs (Fig. 1c-e) and flow cytometry (Th1: [16.72 \pm 6.33] % vs. HCs [8.61 \pm 6.59] %, $p < 0.01$; Th17: [4.05 \pm 1.83] % vs. [1.94 \pm 1.02] %, $p < 0.001$) (Fig. 1f-h), establishing immune dysregulation as a therapeutic target. To address this imbalance, we systematically profiled MSC from eight human tissues (umbilical cord [UC], dental pulp [DP], etc.), all conforming to ISCT standards: CD14⁺/CD19⁺/CD34⁺/CD45⁺/HLA-DR ≤ 2 % purity, CD44⁺/CD73⁺/CD90⁺/CD105⁺ ≥ 95 % purity (FACS) (Supplementary Table 4, Supplementary Fig. 1 [Fig. S1]), and trilineage differentiation confirmed (Fig. S2). RNA sequencing of 24 donors ($n = 3$ /tissue type) uncovered hierarchically organized heterogeneity - inter-tissue variations outweighed intra-tissue donor differences (Fig. 1i). Tissue origin dictated functional divergence, with ssGSEA pathway analysis exposing DPMSC unique Th1/Th17 modulation signature (DPMSC vs. UCMSC, FDR = 0.0078557 for Th1; FDR = 6.372116e-06 for Th17; Fig. 1j-k), while maintaining high proliferative capacity across eight cell types (Fig. 1l-m). This heterogeneity may underlie the observed differences in multilineage differentiation potential and immunomodulatory capacity, which contribute to varying therapeutic effects in different disease contexts. Functional prioritization through MSC-PBMC co-cultures demonstrated that DPMSC exceptional immunoregulatory effects, and significant differences were identified in its ability to modulate Th1 and Th17 responses compared to UCMSC, while maintaining similar proliferative rates. As candidate cells, under Th1/Th17-polarizing conditions, DPMSC reduced the Th1 subset by (61.30 \pm 2.34) % and the Th17 subset by (54.73 \pm 7.05) % compared to UCMSC ($p < 0.001$; Fig. 1n-q). Previous studies have shown that MSC can alleviate various diseases by regulating the balance between Th1, Th17, and Treg populations [45,46]. Therefore, we also assessed the differences in the ability of UCMSC and DPMSC to regulate the Treg subset in PBMCs, and found that both had similar effects in promoting Treg proliferation (Fig. S3).

3.2. DPMSC outperform UCMSC in TNBS-induced colitis through immunomodulation

Transcriptomic profiling of tissue-specific MSC revealed DPMSC's distinct immunoregulatory signature, characterized by 2.01-fold elevated *IL10* expression ($p < 0.01$) and reduced pro-inflammatory mediators (*IDO* 46.7 %, *CCL2* 39.40 %; $p < 0.001$) compared to UCMSC (Fig. 2a). Co-culture with PBMCs under Th1/Th17-polarizing conditions demonstrated DPMSC's superior capacity to suppress pathogenic cytokines of PBMCs, attenuating IFN- γ , IL8, IL17 A, and TNF transcription and expression versus UCMSC ($p < 0.05$; Fig. 2b-c), establishing their enhanced paracrine potency. After obtaining significant support from in vitro experiments, we investigated the differences in therapeutic efficacy of different cell interventions in an inflammatory model animal. Mice were fasted for 24 h prior to CD induction, followed



(caption on next page)

Fig. 3. In vitro Evaluations of Th1/17 differential significant gene TLR5 mediated CD4⁺ T cell differentiation.

(a) A bubble plot was created to visualize the KEGG enrichment analysis results for immune-related pathways that were significantly enriched in the DEGs between UCMSC and DPMSC. (b) Volcano plots displaying up- and down-regulated immune-related genes in UCMSC and DPMSC. (c) A gene expression heatmap was created to illustrate the expression levels of DEGs related to Th1 and Th17 between UCMSC and DPMSC. The color of each square indicates the scaled expression level of the corresponding gene. Each column represents a sample, while each row represents a DEG related to Th1 or Th17. (d) Genes associated with Th1 and Th17 differentiation, identified through genomic screening, were validated by q-PCR. (e) Gene expression discrepancy of TLRs family members between DPMSC and UCMSC. (f) Boxplot for TLR5 expression of eight tissues derived MSC. (g) Significant differences in Th1/Th17-related membrane genes between UCMSC and DPMSC, with a focus on TLR5, a membrane protein. (h, i) Western blotting and quantitative analysis of TLR5 protein expression in UCMSC and DPMSC derived from different individuals. (j, k) Western blotting and quantitative analysis of TLR5 protein expression in UCMSC and DPMSC transfected with SiTLR5 were performed. (l-o) Representative flow cytometry analysis of CD4⁺ T cell differentiation into Th1 and Th17 cells in PBMCs following different treatments, along with corresponding quantitative analysis. UCMSC and DPMSC suppress Th1 (CD3⁺CD8⁻IFN γ ⁺) and Th17 (CD3⁺CD8⁻IL17 A⁺) differentiation reversed upon TLR5 knockout. *p* values: **p* < 0.05, ***p* < 0.01, ****p* < 0.001.

by TNBS administration via the anus on day 0 (D0) modeling human CD endotypes. Six hours and 24 h post-administration, MSC were injected into the abdominal cavity and tail vein, respectively, and all mice were euthanized on day 4 (D4) (Fig. S4). To facilitate live cell tracking, UCMSC and DPMSC were labeled with GFP and CM-DiI before transplantation. The results demonstrated that MSC were widely distributed in the colonic region of the mice between 6 and 72 h following tail vein injection (Fig. S5), correlating with accelerated clinical recovery. Mechanistically, mRNA and cell subset analyses showed that DPMSC reprogrammed CD4⁺ T cell polarization towards Th1/Th17 in various immune regions. Flow cytometry confirmed the systemic immunomodulation of DPMSC: CD4⁺ T cells from MLN showed a reduction of (37.31 ± 10.56) % in IFN- γ ⁺ and (42.01 ± 2.15) % in IL-17 A⁺ populations (vs. UCMSC; *p* < 0.05; Fig. S6a, Fig. S7a-b and Fig. 2d-e); CD4⁺ T cells from the spleen showed a reduction of (34.78 ± 3.84) % in IFN- γ ⁺ and (51.56 ± 8.45) % in IL-17 A⁺ populations (vs. UCMSC; *p* < 0.05; Fig. S6b, Fig. S7c-d and Fig. 2f-g). However, the proportion of CD4⁺IL4⁺ cells in both MLN and spleen showed no statistical difference (*p* > 0.05; Fig. S8). DPMSC-treated mice regained 103.1 % of baseline weight by D4 versus 97.74 % for UCMSC (*p* < 0.01; Fig. 2h), alongside a significant difference in DAI scores on both day 2 and day 3 (*p* < 0.05; Fig. 2i). Colon shortening – hallmark of TNBS-induced damage – was reversed to (77.43 ± 3.82) % of healthy controls with DPMSC versus (70.74 ± 3.49) % for UCMSC (*p* < 0.05; Fig. 2j, m). Histopathological quantification validated DPMSC's mucosal repair capacity: H&E/PAS/MPO staining showed a more significant crypt architecture restoration and higher goblet cell density compared to the UCMSC group (Fig. 2k, n-p). Neutrophilic infiltration, measured by MPO activity, was reduced to near-homeostatic levels (Δ 68.65 % vs. CD controls) with DPMSC versus Δ 30.00 % for UCMSC (*p* < 0.001; Fig. 2l). This multi-tiered regulation – combining pathogenic subset inhibition and regulatory network activation – positions DPMSC as precision cellular therapeutics for Th1/Th17-associated pathologies.

3.3. Lineage-specific TLR5 surfaceome contributes to MSC immunomodulatory function: A mechanistic determinant of divergent T-helper cell polarization and differentiation

To identify the key target genes of UCMSC and DPMSC that contribute to their differential therapeutic effects and varying regulation of Th cell differentiation in TNBS-CD mice, we further analyzed the RNA sequencing from MSC of 6 donors (3 donors per tissue type). KEGG enrichment of DPMSC and UCMSC specific DEGs (Fig. 3a) mapped to T cell differentiation signaling (FDR = 3.434405e-2) and IBD pathway (FDR = 1.042496e-2), mechanistically linking their tissue-specific epigenome to enhanced clinical potential. Multi-omics integration delineated tissue-specific differences between UCMSC and DPMSC in genes related to Th1/Th17 immune differentiation (Fig. 3b-c). Multi-platform

cross-validation of the principal Th1/Th17-associated transcriptome divergences confirmed *TLR5* as the dominant lineage-defining signature in DPMSC, exhibiting (48.3 ± 7.7)-fold elevated mRNA abundance versus UCMSC (*p* < 0.001; Fig. 3d). *TLR5* demonstrated lineage-specific dominance across TLR-family members (Δ log2FC > 3.993504 vs. *TLR1/3/4/6*; *p* < 0.001; Fig. 3e), with gene expression data positioning DPMSC *TLR5* at the immunoregulatory apex among eight MSC types (*p*_{av} = 0.000792; Fig. 3f). Correlation analysis of Th1/Th17-related immune genes and cell membrane genes mechanistically linked *TLR5* to Th1/Th17 modulation: suppression of Th1/Th17 drivers (Fig. 3g). Consequently, *TLR5* was identified as a key target membrane gene for further study. Protein analysis via Western blot confirmed that *TLR5* protein levels in DPMSC were 2.5 times higher than in UCMSC across different donors (*n* = 3, *p* < 0.05; Fig. 3h, i). To establish a *TLR5*-dependent causality in MSC-driven Th cell polarization divergence, we performed a spatiotemporal loss-of-function assay using three pairs of siRNA hairpins, optimizing *TLR5* knockdown at 72 h and determining the optimal sequences for different cell types (Fig. S9). After 72 h of siRNA transfection, *TLR5* knockdown efficiency was (68.0 ± 3.0) % in DPMSC and (66.2 ± 6.4) % in UCMSC (Fig. 3j, k). We next examined the impact of *TLR5* knockdown on the immunomodulatory capacity of MSC to regulate CD4⁺ T cell differentiation. Expression attenuation of *TLR5* (via validated siRNA) drove the alteration of pro-inflammatory polarization in tri-dimensional PBMCs co-cultures, with DPMSC-SiTLR5 exhibiting a restoration of (12.9 ± 7.6) % Th1 (CD3⁺CD8⁻IFN γ ⁺) subset suppression and (5.4 ± 1.1) % Th17 (CD3⁺CD8⁻IL17A⁺) subset suppression versus control, and with UCMSC-SiTLR5 exhibiting a restoration of (8.8 ± 3.8) % Th1 (CD3⁺CD8⁻IFN γ ⁺) subset suppression and (10.1 ± 1.2) % Th17 (CD3⁺CD8⁻IL17A⁺) subset suppression versus control (Fig. 3 l-o). Strikingly, *TLR5* suppression failed to induce regulatory convergence in Th2 commitment (Fig. S10), underscoring its polarization-selective regulatory dominance. Finally, to assess whether *TLR5* deficiency affects the therapeutic efficacy of MSC in TNBS-CD mice, we treated mice with MSC-SiTLR5 (Fig. S11). Firstly, we further analyzed the immune cell subsets in the spleen and MLNs of different treatment groups after TNBS induction. The results showed that *TLR5*-silenced MSCs restored the suppression of Th1/Th17 subsets compared to the NC group MSCs (*p* < 0.05; Fig. 4a-e). In vivo comprehensive evaluation of MSC-SiTLR5 in TNBS-colitis models demonstrated therapeutic attenuation, with MSC-SiTLR5 grafts showing reduced body weight recovery (UCMSC-SiTLR5, 12.3 %; DPMSC-SiTLR5, 10.7 %; *p* < 0.001 Fig. 4e, f), elevated colonic inflammation severity (Fig. 4g), and shortened colon shortening (UCMSC-SiTLR5, 11.8 %; DPMSC-SiTLR5, 9.6 %; *p* < 0.001; Fig. 4h, i). Histopathological stratigraphy confirmed *TLR5*-dependent mucositis rescue – MSC-SiNC treated colons exhibited superior crypt restitution and goblet cell repopulation, whereas MSC-SiTLR5 groups exhibited an increase in MIO score (Fig. 4j, k). Integrative CD remission indices conclusively positioned *TLR5* as the mechanistic keystone governing

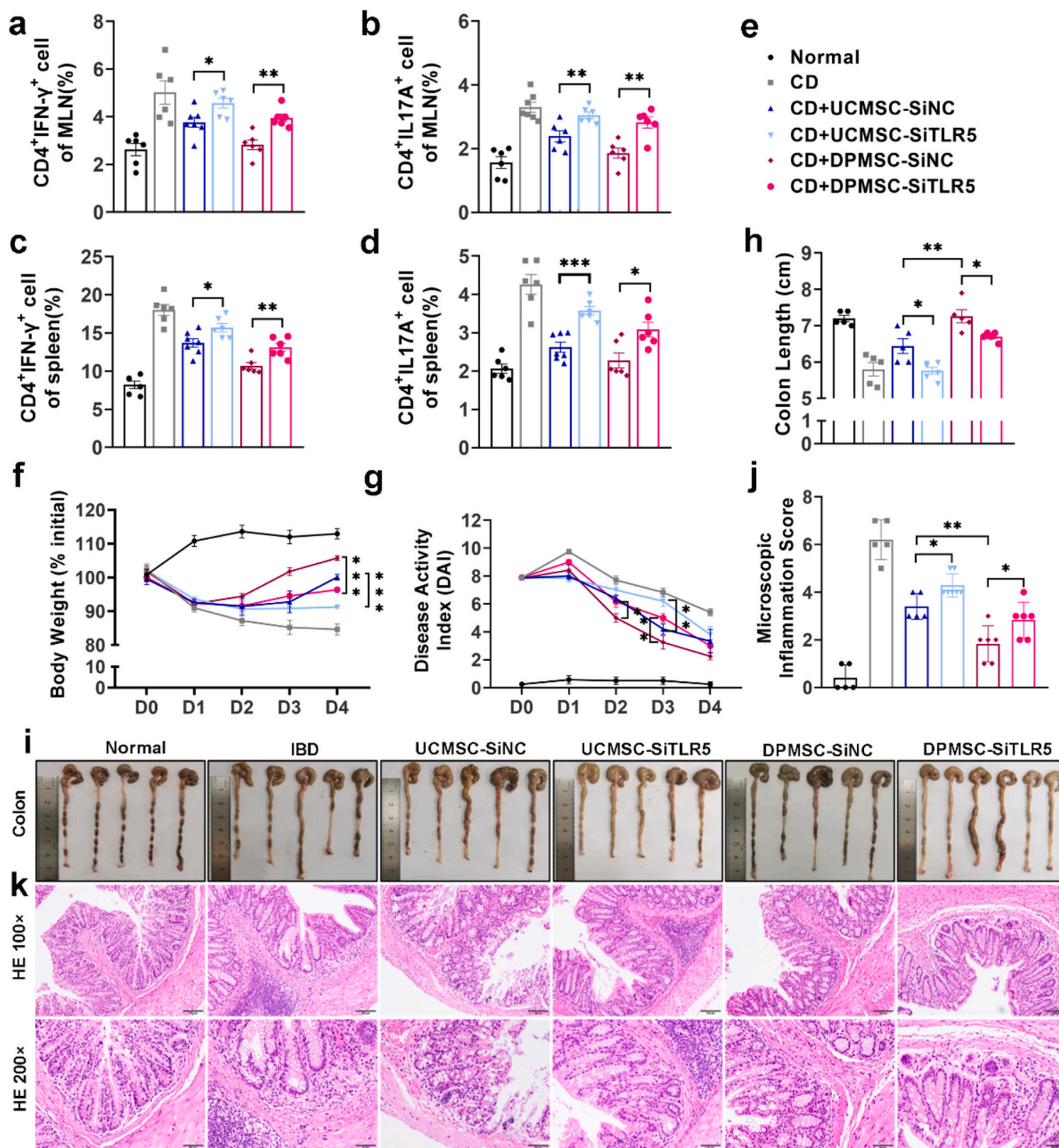
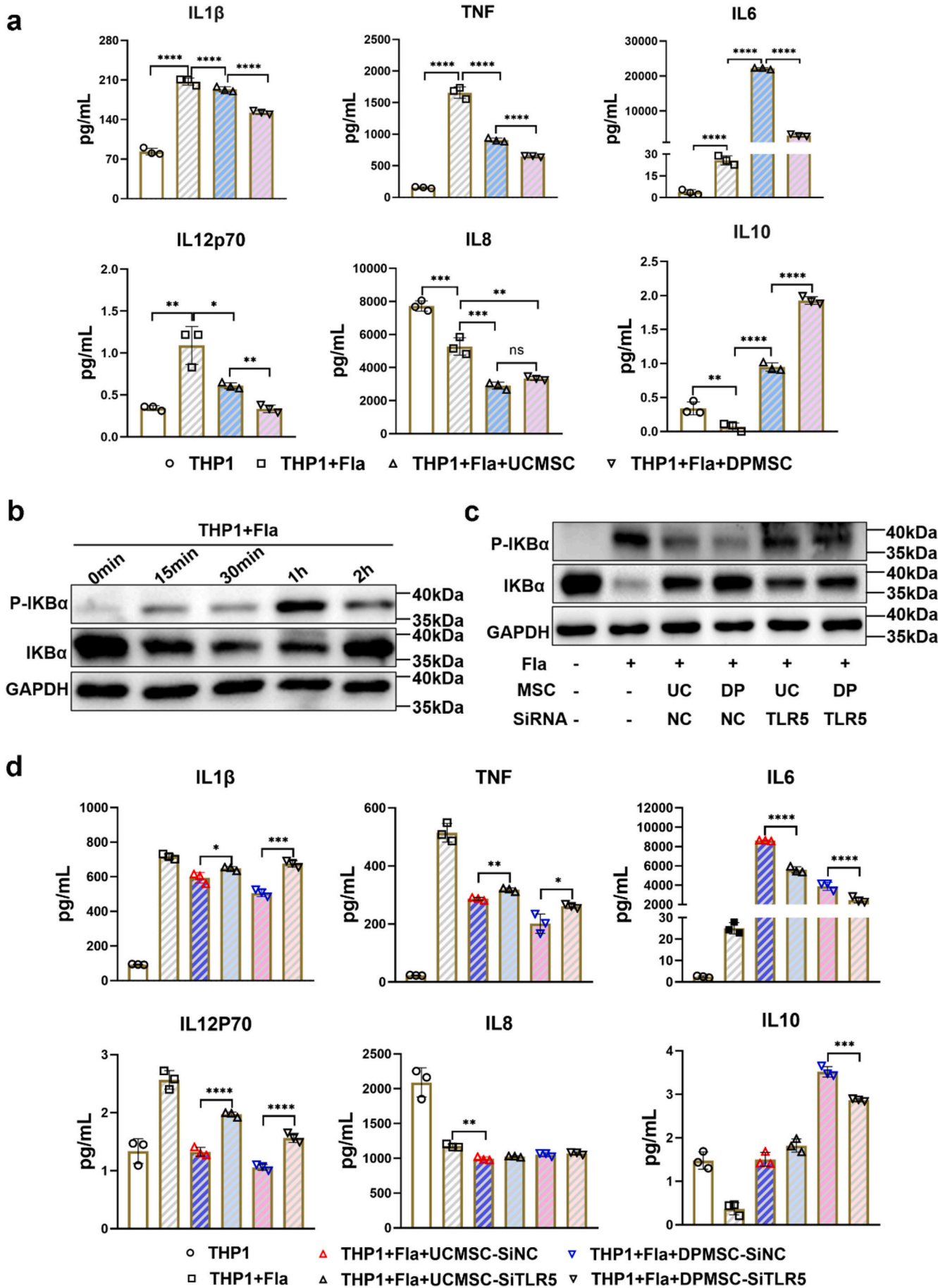


Fig. 4. TLR5-mediated regulation of CD4⁺ T cell fate was further validated in vivo within an CD mouse model.

(a-e) Flow cytometric analysis of proinflammatory T-cell subsets (Th1: CD4⁺IFN- γ ⁺ and Th17: CD4⁺IL-17A⁺) in MLN (a-b) and splenic (c-d) from TNBS-induced CD mice. SiTLR5-MSC administration significantly restored the suppression of Th1 and Th17 responses compared to SiNC-MSC treatment. Statistical significance was determined using ANOVA followed by Tukey's post hoc test. (f-g) Statistical analysis of body weight and DAI in mice after different treatments. (h-i) Images of mouse colon following different treatments, with corresponding statistical analysis of colon length. (j-k) H&E-stained images of mouse colon after different treatments and statistical analysis of MIO scores. The therapeutic effect of MSC on TNBS-induced CD mice is reduced after TLR5 knockout compared to normal MSC. Scale bars: 100 μ m. Significance determined by one-way ANOVA with Tukey's post hoc test; data = mean \pm SD (n = 5–7 biologically independent samples). p values: * p < 0.05, ** p < 0.01, *** p < 0.001.



(caption on next page)

Fig. 5. TLR5-Dependent Crosstalk Between MSC and Macrophages: elucidating key immunoregulatory circuits in vitro.

(a) CBA quantification of Th1/Th17-associated cytokines demonstrates DPMSC more effectively inhibiting secretion of pro-inflammatory IL1 β , TNF, and IL12p70, promoting anti-inflammatory IL10 than UCMSC. (b) Kinetic activation of NF- κ B in Fla-stimulated THP-1 cells: Western blotting reveals time-resolved I κ B α phosphorylation (p-I κ B α /I κ B α ratio peaks at 60 min). (c) Western blot analysis of P-I κ B α and I κ B α in THP-1 co-culturing with normal MSC or TLR5 deficient MSC, with GAPDH used as a housekeeping standard. MSC-mediated NF- κ B blockade: Co-culture with DPMSC reduces p-I κ B α outperforming UCMSC. The blocking of P-I κ B α in THP-1 cells stimulated with Fla. is weakened after TLR5 knockout in MSC. (d) Quantitative statistical analysis of Th1 and Th17-related pro-inflammatory factor protein expression in THP-1 cells treated with TLR5 knockdown MSC. The ability of MSC with TLR5 knockdown to suppress the expression of pro-inflammatory factors in THP-1 cells is significantly restored. *Statistical significance determined by one-way ANOVA with Tukey's post hoc test. Data = mean \pm SD. * p < 0.05, ** p < 0.01, *** p < 0.001, **** p < 0.0001; ns, not significant.

MSC therapeutic potency.

3.4. TLR5-dependent ligand sequestration by MSC reprograms macrophage NF- κ B dynamics to alleviate IBD

TLR5, a membrane protein critical to the innate immune system, is expressed on various mononuclear cells, including macrophages and MSC [47,48]. It is hypothesised that TLR5, which is abundantly expressed on MSC, is able to inhibit T cell proliferation and differentiation plays a critical role in modulating immune responses by competitively binding to PAMPs and Damage-Associated Molecular Patterns (DAMPs) (e.g., free TLR5 ligands). This interaction is thought to inhibit T cell proliferation and differentiation by preventing the activation of the TLR5 signaling pathway in immune cells. As a result, the release of pro-inflammatory cytokines, which could otherwise influence the differentiation of CD4⁺ T cells, is reduced. Systematic interrogation of TLR5-mediated crosstalk between MSC and macrophages uncovered a ligand competition axis underpinning MSC therapeutic efficacy in IBD. Spatial proteomic profiling confirmed constitutive TLR5 surface expression on both UCMSC and DPMSC, as well as THP-1-derived macrophages. Mechanistic dissection using Fla-challenged trans-well co-cultures revealed: DPMSC demonstrated superior inflammatory suppression compared to UCMSC, as evidenced by significant reductions in the transcriptional and protein levels of key pro-inflammatory cytokines. Specifically, DPMSC inhibited IL-1 β ([26.46 \pm 1.58] % vs. UCMSC, p < 0.0001), TNF α ([60.99 \pm 0.76] % vs. UCMSC, p < 0.0001) and IL12p70 ([69.42 \pm 4.14] % vs. UCMSC, p < 0.01), in a THP-1 co-culture system stimulated with Fla., while amplifying IL-10 (+2.03-fold, p < 0.0001). Divergent IL-6 modulation (+7.46-fold vs. DPMSC, p < 0.001) highlighted source-dependent immunoregulatory plasticity (Fig. S12, Fig. 5a). In summary, with the exception of IL-8, all five inflammatory cytokines showed significant differences between DPMSC and UCMSC when co-cultured with THP-1. Previous studies have suggested that PAMP stimulation may enhance TLR5 expression in macrophages. To investigate this further, we assessed TLR5 protein levels in THP-1-derived macrophages following Fla. stimulation. However, our results showed that Fla. did not influence TLR5 expression in THP-1 (Fig. S13). Additionally, Fla. stimulation did not alter the secretion of inflammatory cytokines by MSC (Fig. S14). These findings indicate that the observed changes in inflammatory factor production within the THP-1-MSC co-culture system are likely due to competitive binding of TLR5 ligands between MSC and macrophages, rather than an upregulation of TLR5 expression. Since TLR5 is abundantly expressed on THP-1 membranes, enabling efficient recognition of PAMPs and DAMPs to initiate innate immune cascades. Mechanistically, TLR5 recruits the adaptor protein MyD88 upon ligand binding, triggering canonical NF- κ B pathway activation—a process central to inflammatory cytokine/chemokine production. Under basal conditions, NF- κ B heterodimers are sequestered in the cytoplasm via tight association with inhibitory I κ B proteins. Ligand engagement catalyzes I κ B kinase (IKK)-mediated I κ B α phosphorylation, marking it for proteasomal degradation. This liberates NF- κ B to translocate into the nucleus, where it drives transcription of pro-inflammatory mediators. To resolve the kinetics of TLR5-induced NF- κ B signaling, THP-1-derived macrophages were stimulated with Fla. over a time course (15 min – 2 h). Time-resolved immunoblotting pinpointed I κ B α phosphorylation peaking at 1 h post-Fla.

Phosphorylation levels declined by 2 h, reflecting dynamic feedback regulation of the pathway (Fig. 5b). We then analyzed the changes in I κ B α and P-I κ B α in THP-1 co-cultured with MSC 1 h after Fla. stimulation with DPMSC demonstrating a more pronounced inhibitory effect (Fig. S15). Notably, pharmacological inactivation of TLR5 via siRNA transfection (Si-TLR5) in UCMSC and DPMSC abrogated their capacity to suppress P-I κ B α phosphorylation, restoring macrophage NF- κ B activation (Fig. 5c). Concomitantly, genetic ablation of TLR5 in MSC markedly elevated proinflammatory cytokine secretion (IL-1 β , TNF, and IL-12p70) in THP-1 co-culture supernatants relative to MSC-SiNC controls (Fig. 5d). Moreover, we systematically profiled activation kinetics in the canonical MAPK cascade following Fla. stimulation. Time-resolved immunoblotting revealed rapid phosphorylation of JNK and p38 kinases in THP-1, peaking at 1 h post-stimulation (Fig. S16a), while ERK phosphorylation remained unperturbed under identical conditions. Remarkably, co-culture with UCMSC or DPMSC demonstrated no discernible attenuation of JNK or p38 phosphorylation in THP-1-derived macrophages relative to MSC-free controls (Fig. S16b). Collectively, these findings provide direct evidence that TLR5 expression in MSC is indispensable for their paracrine modulation of NF- κ B pathway activity in macrophages, positioning TLR5 as a critical molecular mediator of MSC-driven immunoregulatory functions. To further validate our hypothesis and assess the role of macrophages in MSC-mediated IBD treatment, we depleted macrophages in IBD mice (Fig. S17) and compared the therapeutic effects of UCMSC and DPMSC. Macrophage depletion abolishes MSC therapeutic stratification in vivo: Clodronate-induced macrophage clearance (spleen: F4/80⁺ ↓88.5 %; MLN: F4/80⁺ ↓65.1 %, Fig. 6b-d) negated DPMSC efficacy advantages in: (1) Clinical metrics: Weight recovery (Δ = 3.2 % UCMSC vs. DPMSC, p = 0.14; Fig. 6e, g), DAI scores (3.6 vs. 2.8, p = 0.11; Fig. 6f, g). (2) Histopathology: Colon shortening ([6.01 \pm 0.32] vs. [6.04 \pm 0.21] cm, p = 0.73), MPO activity (p = 0.22; Fig. 6h-k). (3) Crypt architecture restoration and goblet cell regeneration (Fig. 6l-n) aligned post-macrophage ablation. TLR5-mediated ligand scavenging has been established as the hierarchical driver of mucosal resolution.

In summary, our multi-parametric profiling establishes a subtype of MSC with high TLR5 expression (TLR5^{hi}-MSC) as a functionally stratified subtype, capable of competitively binding to Fla. in intestinal macrophages, effectively blocking TLR5/NF- κ B signalosome assembly and reprogramming gut immune networks, leading to superior therapeutic precision in IBD.

3.5. TLR5^{hi}-MSC-CMNP exhibit clinically relevant immunoregulatory efficacy with enhanced biosafety

Through systematic interrogation of tissue-specific MSC transcriptomes, we found that Th1/Th17 modulatory capacity exhibited striking covariation with membrane protein signatures across MSC subtypes. Crucially, membrane fractions isolated from mechanically lysed MSC recapitulated the immunosuppressive potency of viable MSC systems in CD4⁺ T cell polarization assays. Quantitative CFSE-based proliferation assays demonstrated that MSC membrane fragments robustly suppressed PBMCs expansion (Figs. S16a-b), while concurrently amplifying regulatory Treg populations and attenuating differentiation of CD4⁺ T cells into pro-inflammatory Th1/Th17 subsets (Figs. S16c-f). To overcome limitations inherent to live-cell

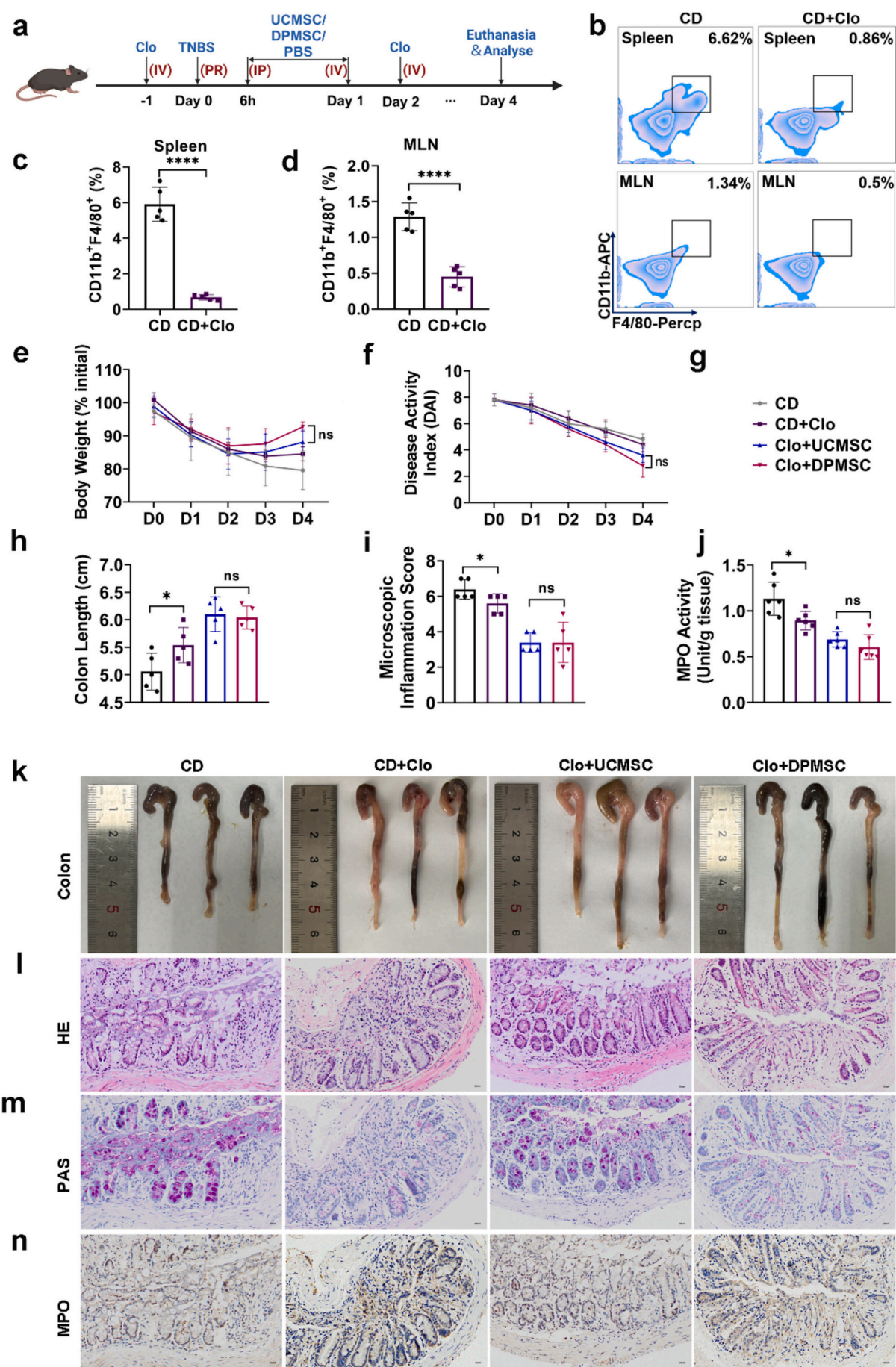


Fig. 6. TLR5-dependent crosstalk between MSCs and macrophages in modulating Th1/Th17 responses were further supported by CD mouse model.

(a) Time course of TNBS and PBS/UCMSC(SiNC/SiTLR5)/DPMSC(SiNC/SiTLR5) treatment. (b-d) Representative flow cytometry analysis of CD11b⁺F4/80⁺ M1 cells in the spleen and MLN following Clodronate treatment, with corresponding quantitative analysis. (e-k) Statistical analysis of body weight, DAI, colon length, and MIO in IBD mice after different treatments. (l-n) Images and pathological staining (HE, PAS, and MPO) of the colon from CD mice after various treatments. Scale bars: 100 μ m. When macrophages were depleted, DPMSC no longer exhibited greater improvement in IBD compared to UCMSC. *Statistical significance determined by one-way ANOVA with Tukey's post hoc test. Data = mean \pm SD. * $p < 0.05$, ** $p < 0.01$, *** $p < 0.001$, **** $p < 0.0001$; ns, not significant.

administration, we developed MSC-CMNP — a standardized nanoparticle platform generated via extrusion-based membrane fractionation. Transmission electron microscopy (TEM) and Dio-based fluorescence imaging confirmed MSC-CMNP exhibited monodisperse spherical nanostructures ([200–250] nm diameter; Fig. 7a-b), contrasting sharply with polydisperse membrane aggregates from naive lysates. Flow cytometric profiling validated retention of MSC-specific surface markers (CD90/CD73 > 95 %; Fig. 7c), while zeta potential ($- [25.3 \pm 2.1]$ mV) and dynamic light scattering (DLS) analyses revealed colloidal stability over 14 days (Fig. 7d-e), underscoring homogeneity and batch-to-batch reproducibility. To further validate the biochemical and functional characteristics of MSC-CMNP, Immunoblotting analysis were conducted and revealed that (1) Absence of calnexin (endoplasmic reticulum marker), excluding organelle contamination; (2) Enrichment of tetraspanins (CD81) and membrane markers (TSG101); (3) High expressivity of CD90, corroborating MSC membrane specificity. Critically, TLR5 — a pivotal mediator of MSC immunoregulation — exhibited higher expression on DPMSC-CMNP (DP-CMNP) compared to UCMSC-CMNP (UC-CMNP), consistent with levels seen in live cells (Fig. 7f), mechanistically linking membrane composition to functional potency. In vitro functional assays demonstrated MSC-CMNP: (1) selectively inhibited Th1/Th17 polarization (Fig. 7g-i), key drivers of CD; (2) competitively disrupted Fla-macrophage interactions via TLR5, suppressing M1 polarization (Fig. S18a-b); (3) primed an anti-inflammatory milieu that attenuated Th1/Th17 skewing in CD4⁺ T cells (Fig. S19a-b). Binding specificity was confirmed by: (1) TLR5-dependent Fla. sequestration: Anti-TLR5 antibodies blocked >70 % of MSC-CMNP–Fla interactions (Fig. 7j-k, S20a-b), indicating TLR5-mediated interception of PAMPs; (2) spatiotemporal Fla. competition: confocal live imaging revealed MSC-CMNP displaced Fla. from CM-Dil-labeled macrophages (Fig. S20c). Then, we have conducted additional experiments using human primary macrophages (pM ϕ) derived from PBMCs, isolated from healthy donors. The purity of CD14⁺ monocytes was confirmed by FCM using CD11b, CD14, and CD45 markers (Fig. S21). We then repeated key experiments previously performed in the THP-1 system to assess the immunomodulatory effects of MSC-derived TLR5^{high}-CMNPs. These included: (1) Evaluation of macrophage polarization (M1/M2) following stimulation with different types of CMNPs (e.g., UC-SiNC-CMNP, UC-SiTLR5-CMNP, DP-SiNC-CMNP, DP-SiTLR5-CMNP), with or without Fla. (2) Investigation of TLR5-mediated effects using CMNPs pre-incubated with anti-TLR5 neutralizing antibodies. (3) Assessment of downstream Th1/Th17 polarization in PBMCs stimulated with the macrophage-conditioned supernatant. The macrophage phenotype was analyzed by FCM using surface markers CD11b, CD86, and CD206, with the gating strategy shown in Fig. S22. The corresponding experimental results are presented in the revised Fig. 7l-m, demonstrating that CMNPs competitively bind to Fla. via a TLR5-dependent mechanism to modulate macrophage polarization, thereby influencing the Th1/Th17 immune axis. These findings are highly consistent with the results obtained from our previous experiments using THP-1 cells. We have included a mechanistic illustration in Fig. S23.

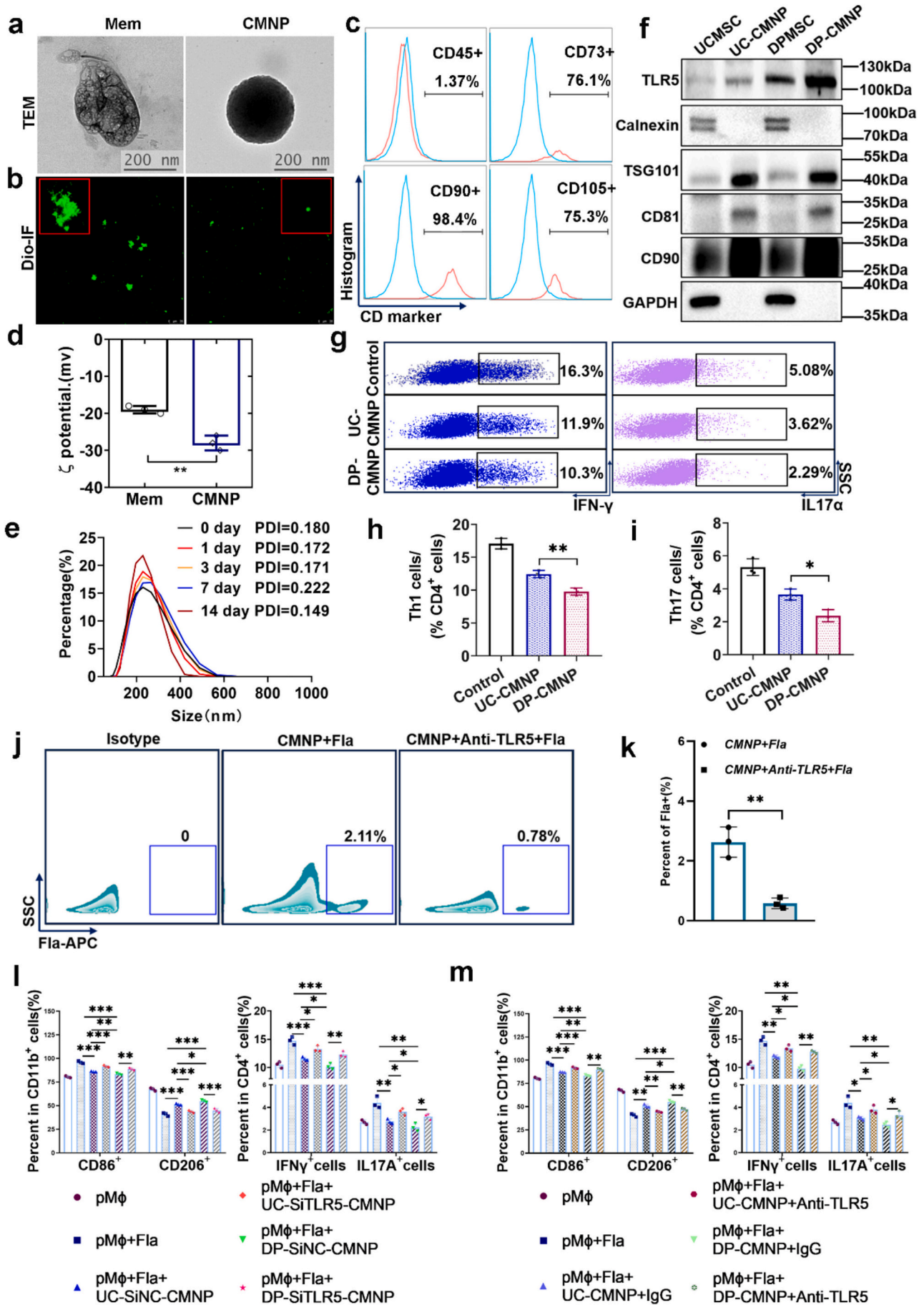
Building upon this molecular paradigm, we engineered TLR5-enriched biomimetic nanoparticles (DP-CMNP) derived from TLR5^{hi}-MSC as pathogen receptor-mimetic vesicles, contrasting with TLR5^{low}-

MSC-derived controls (UC-CMNP). Systematic evaluation in TNBS-challenged mice (Fig. 8a), intraperitoneal MSC-CMNP: (1) Achieved colon-specific biodistribution within 12 h (Video S1, Fig. 8b); (2) We first performed immunofluorescence staining of CD86/Arg-1 (M1/M2) on colon tissues from different treatment groups. The results showed that the CMNP treatment groups inhibited the increase of M1 macrophages in the colon and promoted the proportion of M2 macrophages. However, the proportion of M1 macrophages in the colon of the DP-CMNP group was higher than that in the UC-CMNP group (Fig. 8c); (3) Cell subset analysis showed that DP-CMNP could also program the polarization direction of CD4⁺ T cells in multiple immune regions, skewing them towards Th1/Th17. Flow cytometry confirmed the role of DP-CMNP in systemic immune modulation: Among CD4⁺ T cells from the MLN, the percentage of IFN- γ ⁺ cells was reduced by (36.74 ± 8.07) % and IL-17 A⁺ cells was reduced by (37.71 ± 14.90) % (vs. UCMSC; $p < 0.05$; Fig. 8d-e); Among CD4⁺ T cells from the spleen, the percentage of IFN- γ ⁺ cells was reduced by (35.85 ± 7.43) % and IL-17 A⁺ cells was reduced by (36.21 ± 9.43) % (vs. UCMSC; $p < 0.05$; Fig. 8f-g); (4) Ameliorated CD pathology: DP-CMNP outperformed UC-CMNP in restoring colon length ($p < 0.001$), normalizing disease activity indices (DAI/weight loss; Fig. 8h-m), and reducing histopathological scores (H&E/MIO/MPO; Fig. 8n-q); (3) Mimicked the therapeutic efficacy of live MSCs while avoiding concerns related to uncontrolled proliferation or ectopic engraftment.

This nano-bioengineering strategy validates functional inheritance of MSC membrane signatures while overcoming translational bottlenecks in cell therapy manufacturing and provides a comprehensive mechanistic framework and solid theoretical foundation for addressing the membrane source selection challenge in CMNP development. These results offer compelling evidence to advance MSC-CMNP formulations as promising candidates for clinical application as personalized immunomodulators.

4. Conclusion

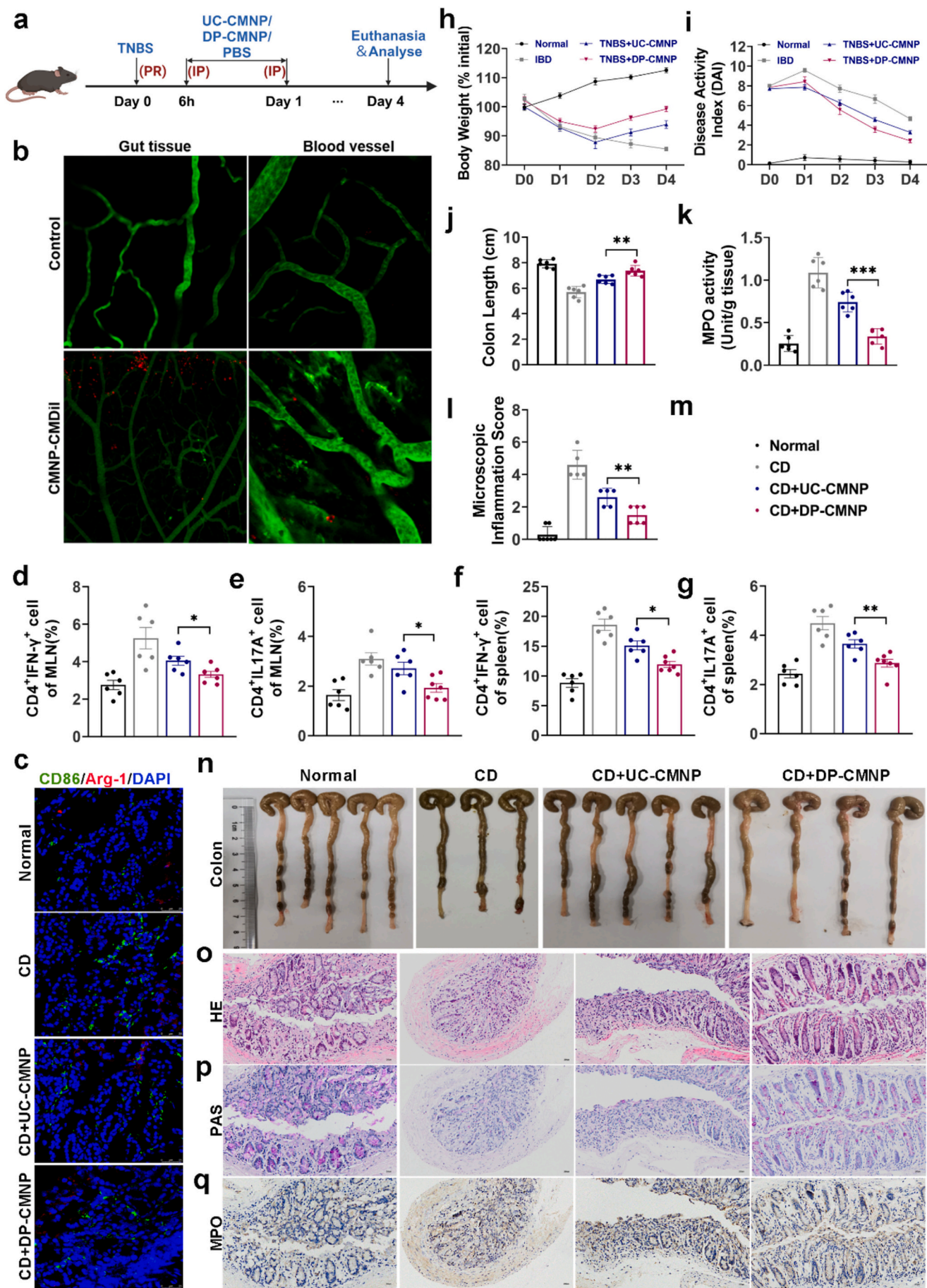
This study establishes that DP-derived TLR5^{hi} MSCs (DPMSC) uniquely resolve CD-associated Th1/Th17 immune dysregulation through competitive interception of the pathogenic Fla/TLR5/NF- κ B axis in gut macrophages. By integrating systems biology and functional screening, we identified TLR5 membrane enrichment as the critical determinant of DPMSC's superior immunomodulatory capacity, outperforming conventional MSCs (e.g., UCMSC) in reprogramming T-cell homeostasis and reversing colitis pathology. The development of a decellularized MSC membrane-derived nanoparticle platform (TLR5^{hi}-CMNP) recapitulated DPMSC's therapeutic efficacy while overcoming limitations associated with cell viability dependence, achieving sustained TLR5/NF- κ B pathway blockade and 68.9 % colon inflammation resolution in preclinical models. Our findings advocate a paradigm shift towards "deconstructed cell therapy," where MSC heterogeneity is leveraged to engineer biomimetic nanomaterials tailored to disease-specific immune checkpoints. We hypothesize that TLR5^{hi}-CMNP's ligand scavenging mechanism may extend to other TLR5-mediated inflammatory disorders, warranting further investigation into its adaptability across immune-driven pathologies. For clinical translation, we



(caption on next page)

Fig. 7. Engineering and Functional Validation of MSC-Derived CMNP for Targeted Immunomodulation in vitro.

(a) TEM reveals uniform monodisperse spherical nanostructures of CMNP. Samples were negatively stained with phosphotungstic acid (2 % w/v). (b) Fluorescent imaging of Dio-labeled CMNP (green fluorescence) demonstrates intact membrane encapsulation and homogeneous dispersion. Scale bars: 200 nm. (c) Immunophenotypic profiling: Flow cytometry confirms CMNP retain MSC-specific surface markers. (d-e) CMNP retained monodisperse characteristics ($PDI < 0.2$) with a sustained negative zeta potential following 14-day refrigerated storage (4 °C), demonstrating robust physicochemical stability. (f) Functional membrane proteomics: Western blotting reveals preserved TLR5 expression on CMNP alongside CD90/TSG101 enrichment, confirming cargo sorting fidelity. (g-i) In vitro immunosuppressive activity: CMNP treatment suppresses Th1/Th17 polarization in PBMCs, with DP-derived CMNP exhibiting stronger inhibitory effects on Th1/Th17 polarization compared to UC-derived CMNP, showing statistical significance. (j-k) Fla. binding specificity of CMNP: FCM statistical analysis showing the binding of APC-labeled Fla. to CMNP, with pre-incubation with anti-TLR5 reducing the APC-Fla signal by 63.0 %. (l-m) The percentages of CD86⁺ (M1-like) and CD206⁺ (M2-like) macrophages (left), and IFN γ ⁺ (Th1) and IL-17 A⁺ (Th17) CD4⁺ T cells (right) under various treatment conditions. In panel l, knockdown of TLR5 in CMNPs (UC-SiTLR5-CMNP and DP-SiTLR5-CMNP) significantly reversed the previously observed suppression of M1 polarization (CD86⁺ pM ϕ) and promotion of M2 polarization (CD206⁺ pM ϕ) compared to pM ϕ + Fla. + control CMNPs. This shift in macrophage consequently reversed the reduction in Th1 (IFN γ ⁺ cells) and Th17 (IL-17 A⁺ cells) polarization. In panel m, functional blockade of TLR5 using neutralizing antibodies (Anti-TLR5) in CMNPs similarly reversed the suppressed M1 polarization and enhanced M2 markers. Correspondingly, the decreased frequencies of IFN γ ⁺ and IL-17 A⁺ CD4⁺ T cells were also reversed. *Statistical significance determined by one-way ANOVA with Tukey's post hoc test. Data = mean \pm SD. * $p < 0.05$, ** $p < 0.01$, *** $p < 0.001$, **** $p < 0.0001$; ns, not significant.



(caption on next page)

Fig. 8. Engineering and Functional Validation of MSC-Derived CMNP for Targeted Immunomodulation in vivo.

(a) Time course of TNBS and PBS/UC-CMNP/DP-CMNP treatments. (b) Schematic representation of in vivo imaging of colonic tissue and blood vessels in CD mice following intraperitoneal injection of CM-DII-labeled CMNP for 12 h. (c) Immunofluorescence staining of CD86/Arg-1 (M1/M2, 488/561) on colon tissues from different treatment groups. (d-g) Flow cytometric analysis of proinflammatory T-cell subsets (Th1: CD4⁺IFN- γ ⁺ and Th17: CD4⁺IL-17 A⁺) in MLN (a-b) and splenic (c-d) from TNBS-induced CD mice. DP-CMNP administration significantly suppressed the Th1 and Th17 responses compared to UC-CMNP treatment. (h-n) Therapeutic effects of CMNP with differential TLR5 protein levels in a murine IBD model. Quantitative improvement of IBD parameters, including colon length recovery, histological inflammation index, MPO activity, body weight loss, and DAI score. (o-q) Representative colonic histopathology: H&E staining shows significantly reduced inflammatory cell infiltration in the DP-CMNP (TLR5^{hi}-CMNP) treatment group, compared to the UC-CMNP (TLR5^{low}-CMNP) group. PAS and MPO staining results are consistent with the H&E staining trend. Scale bar: 100 μ m. *Statistical significance determined by one-way ANOVA with Tukey's post hoc test. Data = mean \pm SD. * $p < 0.05$, ** $p < 0.01$, *** $p < 0.001$, **** $p < 0.0001$; ns, not significant.

recommend prioritizing functional membrane signature screening in MSC source selection and advancing TLR5^{hi}-CMNP as a standardized, scalable cell-free therapeutic to overcome the variability and safety limitations of live-cell therapies.

Supplementary data to this article can be found online at <https://doi.org/10.1016/j.jconrel.2025.114121>.

CRediT authorship contribution statement

Yuanyuan Xie: Visualization, Project administration, Methodology, Funding acquisition, Conceptualization, Writing – review & editing. **Yu Li:** Validation, Methodology, Investigation, Writing – original draft. **Congwang Xu:** Visualization, Validation, Writing – original draft. **Wenting Zhang:** Validation, Investigation. **Yue Jiang:** Software, Investigation. **Liudi Wang:** Software, Resources. **Yingjie Tang:** Software, Resources. **Qing Sun:** Software, Resources. **Hui Yang:** Resources, Funding acquisition. **Xiaoli Mai:** Resources, Funding acquisition. **Pingping Shen:** Supervision, Resources. **Bin Wang:** Supervision, Funding acquisition, Data curation, Writing – review & editing.

Declaration of generative AI and AI-assisted technologies in the writing process

During the preparation of this work, the authors used ChatGPT and DeepSeek in order to gather information for our article, so that we can make it more rigorous and more convincing. After using this tool, the authors reviewed and edited the content as needed and take full responsibility for the content of the publication.

Declaration of competing interest

The authors declare that they have no known competing financial interests or personal relationships that could have appeared to influence the work reported in this paper.

Acknowledgements

This study was supported by National Natural Science Foundation of China [No. 82270701 (Bin Wang), and 82472048 (Xiaoli Mai)], Nanjing Municipal Health Science and Technology Development Special Fund Project [No. YKK23108 (Yuanyuan Xie)], Natural Science Foundation of Jiangsu Province of China [No. BK20230141 (Hui Yang)], Clinical Research Special Fund of Nanjing Drum Tower Hospital [No. 2024-LCYJ-PY-77 (Yuanyuan Xie)]. The authors thank all the tissue donors for MSCs in this study for their collaborative participations.

Data availability

Data will be made available on request.

References

- [1] G.G. Kaplan, The global burden of IBD: from 2015 to 2025, nature reviews, Gastroenterol. Hepatol. (2015), <https://doi.org/10.1038/nrgastro.2015.150>.
- [2] S. Sebastian, B. Siegmund, IBD across the ages—a journey together, J. Crohns Colitis (2024), <https://doi.org/10.1093/ecco-jcc/jjae118>.
- [3] J. Li, A. Ueno, M. Fort Gasia, J. Luidert, T. Wang, C. Hirota, et al., Profiles of Lamina Propria T Helper Cell Subsets Discriminate between Ulcerative Colitis and Crohn's Disease, Inflammatory Bowel Diseases, 2016, <https://doi.org/10.1097/mib.0000000000000811>.
- [4] R. Gomez-Bris, A. Saez, B. Herrero-Fernandez, C. Rius, H. Sanchez-Martinez, J. M. Gonzalez-Granado, CD4 T-cell subsets and the pathophysiology of inflammatory bowel disease, Int. J. Mol. Sci. (2023), <https://doi.org/10.3390/ijms24032696>.
- [5] S. Wirtz, M.F. Neurath, Mouse models of inflammatory bowel disease, Adv. Drug Deliv. Rev. (2007), <https://doi.org/10.1016/j.addr.2007.07.003>.
- [6] A. Giammona, B.G. Galuzzi, E. Imperia, C. Gervasoni, S. Remedì, L. Restaneo, et al., Chronic gastrointestinal disorders and miRNA-associated disease: an up-to-date, Int. J. Mol. Sci. (2025), <https://doi.org/10.3390/ijms26010413>.
- [7] M. Heredia, M. Charrou, R.C.W. Klomberg, M.A. Aardoom, M.M.E. Jongma, P. Kemos, et al., Combined plasma protein and memory T cell profiling discern IBD-patient-immunotypes related to intestinal disease and treatment outcomes, Mucosal Immunol. (2025), <https://doi.org/10.1016/j.mucimm.2024.09.004>.
- [8] J. Torres, J. Halfvarson, I. Rodríguez-Lago, C.R.H. Hedin, T. Jess, M. Dubinsky, et al., Results of the seventh scientific workshop of ECCO: precision medicine in IBD—prediction and prevention of inflammatory bowel disease, J. Crohns Colitis (2021), <https://doi.org/10.1093/ecco-jcc/jjab048>.
- [9] T. Kucharzik, P. Ellul, T. Greuter, J.F. Rahier, B. Verstockt, C. Abreu, et al., ECCO guidelines on the prevention, diagnosis, and Management of Infections in inflammatory bowel disease, J. Crohns Colitis (2021), <https://doi.org/10.1093/ecco-jcc/jjab052>.
- [10] C.L. Li, Y. Leng, B. Zhao, C. Gao, F.F. Du, N. Jin, et al., Human iPSC-MSC-derived xenografts modulate immune responses by inhibiting the cleavage of caspases, Stem Cells (2017), <https://doi.org/10.1002/stem.2638>.
- [11] J.Z. Ko, S. Johnson, M. Dave, Efficacy and safety of mesenchymal stem/stromal cell therapy for inflammatory bowel diseases: an up-to-date systematic review, Biomolecules (2021), <https://doi.org/10.3390/biom11010082>.
- [12] Y. Han, X. Li, Y. Zhang, Y. Han, F. Chang, J. Ding, Mesenchymal stem cells for regenerative medicine, Cells (2019), <https://doi.org/10.3390/cells8080886>.
- [13] A.J. Nauta, W.E. Fibbe, Immunomodulatory properties of mesenchymal stromal cells, Blood (2007), <https://doi.org/10.1182/blood-2007-02-069716>.
- [14] C. Xu, Y. Xie, B. Wang, Genetically modified mesenchymal stromal cells: a cell-based therapy offering more efficient repair after myocardial infarction, Stem Cell Res Ther (2024), <https://doi.org/10.1186/s13287-024-03942-7>.
- [15] F. Kheradmand, S.F. Yasaman Rahimzadeh, S.A. Esmaeili, S.S. Negah, N. K. Farkhad, S.E. Nazari, et al., Efficacy of umbilical cord-derived mesenchymal stem cells and exosomes in conjunction with standard IBD drug on immune responses in an IBD mouse model, Stem Cell Res Ther (2025), <https://doi.org/10.1186/s13287-024-04062-y>.
- [16] D. García-Olmo, M. García-Arriaza, L.G. García, E.S. Cuellar, I.F. Blanco, L. A. Prianes, et al., Autologous stem cell transplantation for treatment of rectovaginal fistula in perianal Crohn's disease: a new cell-based therapy, Int. J. Color. Dis. (2003), <https://doi.org/10.1007/s00384-003-0490-3>.
- [17] Y.L. Si, Y.L. Zhao, H.J. Hao, X.B. Fu, W.D. Han, MSCs: biological characteristics, clinical applications and their outstanding concerns, Ageing Res. Rev. (2011), <https://doi.org/10.1016/j.arr.2010.08.005>.
- [18] T. Zhou, Z. Yuan, J. Weng, D. Pei, X. Du, C. He, et al., Challenges and advances in clinical applications of mesenchymal stromal cells, J. Hematol. Oncol. (2021), <https://doi.org/10.1186/s13045-021-01037-x>.
- [19] Q. Xu, W. Hou, B. Zhao, P. Fan, S. Wang, L. Wang, et al., Mesenchymal stem cells lineage and their role in disease development, Mol. Med. (2024), <https://doi.org/10.1186/s10020-024-00967-9>.
- [20] J. Li, Z. Wu, L. Zhao, Y. Liu, Y. Su, X. Gong, et al., The heterogeneity of mesenchymal stem cells: an important issue to be addressed in cell therapy, Stem Cell Res Ther (2023), <https://doi.org/10.1186/s13287-023-03587-y>.
- [21] Y. Shan, M. Zhang, E. Tao, J. Wang, N. Wei, Y. Lu, et al., Pharmacokinetic characteristics of mesenchymal stem cells in translational challenges, Signal Transduct. Target. Ther. (2024), <https://doi.org/10.1038/s41392-024-01936-8>.
- [22] Y. Han, J. Yang, J. Fang, Y. Zhou, E. Candi, J. Wang, et al., The secretion profile of mesenchymal stem cells and potential applications in treating human diseases, Signal Transduct. Target. Ther. (2022), <https://doi.org/10.1038/s41392-022-00932-0>.
- [23] A. Hoseinzadeh, S.A. Esmaeili, R. Sahebi, A.M. Melak, M. Mahmoudi, M. Hasannia, et al., Fate and long-lasting therapeutic effects of mesenchymal stromal/stem-like cells: mechanistic insights, Stem Cell Res Ther (2025), <https://doi.org/10.1186/s13287-025-04158-z>.

- [24] M.B. Preda, C.A. Neculachi, I.M. Fenyo, A.M. Vacaru, M.A. Publik, M. Simionescu, et al., Short lifespan of syngeneic transplanted MSC is a consequence of in vivo apoptosis and immune cell recruitment in mice, *Cell Death Dis.* (2021), <https://doi.org/10.1038/s41419-021-03839-w>.
- [25] Y. Xie, S. Liu, L. Wang, H. Yang, C. Tai, L. Ling, et al., Individual heterogeneity screened umbilical cord-derived mesenchymal stromal cells with high Treg promotion demonstrate improved recovery of mouse liver fibrosis, *Stem Cell Res Ther* (2021), <https://doi.org/10.1186/s13287-021-02430-6>.
- [26] L. Chen, W. Hong, W. Ren, T. Xu, Z. Qian, Z. He, Recent progress in targeted delivery vectors based on biomimetic nanoparticles, *Signal Transduct. Target. Ther.* (2021), <https://doi.org/10.1038/s41392-021-00631-2>.
- [27] M. Pan, Y. Xu, Y. Wang, Y. Jiang, Y. Xie, C. Tai, et al., The therapeutic efficacy comparison of MSCs derived different tissues unveils anti-apoptosis more crucial than angiogenesis in treating acute myocardial infarction, *Stem Cell Res Ther* (2025), <https://doi.org/10.1186/s13287-025-04378-3>.
- [28] Y. Xie, Q. Yi, C. Xu, Y. Wang, Y. Jiang, Y. Feng, et al., Identifying TNFSF4(low)-MSCs superiorly treating idiopathic pulmonary fibrosis through Tregs differentiation modulation, *Stem Cell Res Ther* (2025), <https://doi.org/10.1186/s13287-025-04313-6>.
- [29] T. Zuo, S.C. Ng, The gut microbiota in the pathogenesis and therapeutics of inflammatory bowel disease, *Front. Microbiol.* (2018), <https://doi.org/10.3389/fmicb.2018.02247>.
- [30] P. Qiu, T. Ishimoto, L. Fu, J. Zhang, Z. Zhang, Y. Liu, The gut microbiota in inflammatory bowel disease, *Front. Cell. Infect. Microbiol.* (2022), <https://doi.org/10.3389/fcimb.2022.733992>.
- [31] I.D. Iliev, A.N. Ananthakrishnan, C.J. Guo, Microbiota in inflammatory bowel disease: mechanisms of disease and therapeutic opportunities, *Nat. Rev. Microbiol.* (2025), <https://doi.org/10.1038/s41579-025-01163-0>.
- [32] A.M. Schoepfer, T. Schaffer, S. Mueller, B. Flogerzi, E. Vassella, B. Seibold-Schmid, et al., Phenotypic associations of Crohn's disease with antibodies to flagellins A4-Fla2 and Fla-X, ASCA, p-ANCA, PAB, and NOD2 mutations in a Swiss cohort, *Inflamm. Bowel Dis.* (2009), <https://doi.org/10.1002/ibd.20892>.
- [33] W.C. Shen, Y.C. Lai, L.H. Li, K. Liao, H.C. Lai, S.Y. Kao, et al., Methylation and PTEN activation in dental pulp mesenchymal stem cells promotes osteogenesis and reduces oncogenesis, *Nat. Commun.* (2019), <https://doi.org/10.1038/s41467-019-10197-x>.
- [34] W. Liu, Y. Xie, T. Gao, F. Huang, L. Wang, L. Ding, et al., Reflection and observation: cell-based screening failing to detect HBV in HUMSCs derived from HBV-infected mothers underscores the importance of more stringent donor eligibility to reduce risk of transmission of infectious diseases for stem cell-based medical products, *Stem Cell Res Ther* (2018), <https://doi.org/10.1186/s13287-018-0920-3>.
- [35] W. Marinello, L. Feng, T.K. Allen, Progesterone inhibit interleukin-1 β -induced matrix metalloproteinase 1 and interleukin 8 expression via the glucocorticoid receptor in primary human amnion mesenchymal cells, *Front. Physiol.* (2020), <https://doi.org/10.3389/fphys.2020.00900>.
- [36] R. Menon, E. Radnaa, F. Behnia, R. Urrabaz-Garza, Isolation and characterization human chorion membrane trophoblast and mesenchymal cells, *Placenta* (2020), <https://doi.org/10.1016/j.placenta.2020.09.017>.
- [37] N. Kamali Simsek, A. Benian, K. Sevgin, Y. Ergun, H. Goksever Celik, S. Karahuseyinoglu, et al., MicroRNA analysis of human decidua mesenchymal stromal cells from preeclampsia patients, *Placenta* (2021), <https://doi.org/10.1016/j.placenta.2021.09.004>.
- [38] Y. Gao, Y. Chi, Y. Chen, W. Wang, H. Li, W. Zheng, et al., Multi-omics analysis of human mesenchymal stem cells shows cell aging that alters immunomodulatory activity through the downregulation of PD-L1, *Nat. Commun.* (2023), <https://doi.org/10.1038/s41467-023-39958-5>.
- [39] Y. Xie, W. Liu, S. Liu, L. Wang, D. Mu, Y. Cui, et al., The quality evaluation system establishment of mesenchymal stromal cells for cell-based therapy products, *Stem Cell Res Ther* (2020), <https://doi.org/10.1186/s13287-020-01696-6>.
- [40] H.S. Kim, Y.M. Shin, S. Chung, D. Kim, D.B. Park, S. Baek, et al., Cell-membrane-derived nanoparticles with Notch-1 suppressor delivery promote hypoxic cell-cell packing and inhibit angiogenesis acting as a two-edged sword, *Adv. Mater.* (2021), <https://doi.org/10.1002/adma.202101558>.
- [41] S. Hänzelmann, R. Castelo, J. Guinney, GSEA: gene set variation analysis for microarray and RNA-seq data, *BMC Bioinform.* (2013), <https://doi.org/10.1186/1471-2105-14-7>.
- [42] T. Wu, E. Hu, S. Xu, M. Chen, P. Guo, Z. Dai, et al., clusterProfiler 4.0: A universal enrichment tool for interpreting omics data, *Innovation (Camb.)* (2021), <https://doi.org/10.1016/j.xinn.2021.100141>.
- [43] C. UniProt, UniProt: the universal protein knowledgebase in 2021, *Nucleic Acids Res.* (2021), <https://doi.org/10.1093/nar/gkaa1100>.
- [44] J. Che, L. Sun, J. Shan, Y. Shi, Q. Zhou, Y. Zhao, et al., Artificial lipids and macrophage membranes Coassembled biomimetic Nanovesicles for antibacterial treatment, *Small* (2022), <https://doi.org/10.1002/smll.202201280>.
- [45] P. Luz-Crawford, M. Kurte, J. Bravo-Alegría, R. Contreras, E. Nova-Lamperti, G. Tejedor, et al., Mesenchymal stem cells generate a CD4⁺CD25⁺Foxp3⁺ regulatory T cell population during the differentiation process of Th1 and Th17 cells, *Stem Cell Res Ther* (2013), <https://doi.org/10.1186/scrt216>.
- [46] C. Gong, L. Chang, X. Sun, Y. Qi, R. Huang, K. Chen, et al., Infusion of two-dose mesenchymal stem cells is more effective than a single dose in a dilated cardiomyopathy rat model by upregulating indoleamine 2,3-dioxygenase expression, *Stem Cell Res Ther* (2022), <https://doi.org/10.1186/s13287-022-03101-w>.
- [47] M.M. Shikhagaie, C.K. Andersson, M. Mori, I. Kortekaas Krohn, A. Bergqvist, R. Dahl, et al., Mapping of TLR5 and TLR7 in central and distal human airways and identification of reduced TLR expression in severe asthma, *Clin. Exp. Allergy* (2014), <https://doi.org/10.1111/cea.12176>.
- [48] J.H. Kwon, M. Kim, S. Um, H.J. Lee, Y.K. Bae, S.J. Choi, et al., Senescence-associated secretory phenotype suppression mediated by small-sized mesenchymal stem cells delays cellular senescence through TLR2 and TLR5 signaling, *Cells* (2021), <https://doi.org/10.3390/cells10010063>.